AFRL-VS-HA-TR-2007-1031

Regionalization of Crustal and Upper Mantle Q Structure in Eastern Eurasia Using Multiple Regional Waves

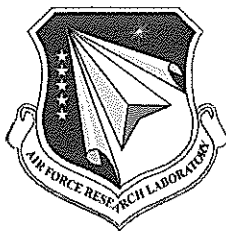James Gaherty
Arthur Lerner-Lam

Lamont-Doherty Earth Observatory of Columbia University
61 Route 9 W
Palisades, NY 10964

Final Report

5 February 2007

AIR FORCE RESEARCH LABORATORY
Space Vehicles Directorate
29 Randolph Road
AIR FORCE MATERIEL COMMAND
Hanscom AFB, MA 01731-3010

NOTICES

Using Government drawings, specifications, or other data included in this document for any purpose other than Government procurement does not in any way obligate the U.S. Government. The fact that the Government formulated or supplied the drawings, specifications, or other data does not license the holder or any other person or corporation; or convey any rights or permission to manufacture, use, or sell any patented invention that may relate to them.

This report was cleared for public release and is available to the general public, including foreign nationals. Qualified requestors may obtain copies of this report from the Defense Technical Information Center (DTIC) (http://www.dtic.mil). All others should apply to the National Technical Information Service.

AFRL-VS-HA-TR-2007-1031 HAS BEEN REVIEWED AND IS APPROVED FOR PUBLICATION IN ACCORDANCE WITH ASSIGNED DISTRIBUTION STATEMENT.

//Signature//   //Signature//

_____   _____
ROBERT J. RAISTRICK   ROBERT BELAND, Chief
Contract Manager   Battlespace Surveillance Innovation Center

This report is published in the interest of scientific and technical information exchange, and its publication does not constitute the Government's approval or disapproval of its ideas or findings.

REPORT DOCUMENTATION PAGE

Form Approved
OMB No. 0704-0188

Public reporting burden for this collection of information is estimated to average 1 hour per response, including the time for reviewing instructions, searching existing data sources, gathering and maintaining the data needed, and completing and reviewing this collection of information. Send comments regarding this burden estimate or any other aspect of this collection of information, including suggestions for reducing this burden to Department of Defense, Washington Headquarters Services, Directorate for Information Operations and Reports (0704-0188), 1215 Jefferson Davis Highway, Suite 1204, Arlington, VA 22202-4302. Respondents should be aware that notwithstanding any other provision of law, no person shall be subject to any penalty for failing to comply with a collection of information if it does not display a currently valid OMB control number. **PLEASE DO NOT RETURN YOUR FORM TO THE ABOVE ADDRESS.**

1. REPORT DATE *(DD-MM-YYYY)* 05-02-2007	2. REPORT TYPE Final Technical Report	3. DATES COVERED *(From - To)* 01-10-2003 – 07-11-2006

4. TITLE AND SUBTITLE
Regionalization of Crustal and Upper Mantle Q Structure in Eastern Eurasia
Using Multiple Regional Waves

5a. CONTRACT NUMBER
F19628-03-C-0122

5b. GRANT NUMBER

5c. PROGRAM ELEMENT NUMBER

6. AUTHOR(S)
James Gaherty, Arthur Lerner-Lam

5d. PROJECT NUMBER

5e. TASK NUMBER

5f. WORK UNIT NUMBER

7. PERFORMING ORGANIZATION NAME(S) AND ADDRESS(ES)

Lamont-Doherty Earth Observatory of Columbia University
61 Route 9W
Palisades, NY 10964

8. PERFORMING ORGANIZATION REPORT NUMBER

9. SPONSORING / MONITORING AGENCY NAME(S) AND ADDRESS(ES)
Air Force Research Laboratory
29 Randolph Road,
Hanscom AFB, MA 01731

10. SPONSOR/MONITOR'S ACRONYM(S)
AFRL

11. SPONSOR/MONITOR'S REPORT NUMBER(S)

12. DISTRIBUTION / AVAILABILITY STATEMENT

13. SUPPLEMENTARY NOTES

14. ABSTRACT
We have mapped lateral variations in seismic Q in eastern Eurasia, including continental China, central Asia, Mongolia and Siberia, using high-frequency regional phases *Lg* and *Pn*, as well as long-period Rayleigh waves. We measured Q of crustal Lg waves in eastern Eurasia using two-station methods. Over 5,000 spectral ratios from 594 interstation paths were used to estimate Lg Q_0 and η (Q at1 Hz and its frequency dependence). These path averages were used to derive tomographic models of Q_0 and η with resolutions between 4 and 10°. The Q_0 model contains values that vary between 100 and 900. Q_0 are the lowest in the Tibetan plateau, increase to moderate levels towards the east and north, and reach maxima in the Siberian and eastern Europe Cratons. Q_0 values correlate well with regional tectonics. Most η values are between 0.14 and 0.50, with a mean of 0.18. These values are lower than those obtained previously. Pn spectra were collected from three seismic experiments in the Tibetan Plateau (TP) over four path groups to study Pn attenuation. A comparison of Pn spectra from these events reveal that mantle lid under north central TP attenuates Pn more severely than under central Asia. Over paths that heavily sample northern TP, Q_0 and η are estimated to be 183±33 and 0.3±0.1. Over paths that sample either a mixture of northern and southern Tibet or eastern Tibet, Q_0 and η are between about 250-270 and 0.0-0.1, respectively. Over the path group that samples easternmost TP the respective estimates are 374±51 and 0.3±0.1. Lateral variation of Pn attenuation inversely correlates with that of the Pn velocity. Possible causes of this variation include (1) a thermally driven mantle Qp, and (2) region-specific velocity structures. We utilized Rayleigh waves with periods longer than ~15 s, derived from regional and near-teleseismic earthquakes, to map lateral variations in crustal and upper-mantle shear velocity and attenuation across eastern Eurasia. In the crust, high values of Q_μ are concentrated in eastern China, extending southward from the north China craton, with a clear low-Q anomaly in the crust beneath northern Tibet. In the upper mantle, the model is characterized by a lid with very high Q values ranging from 250-400, underlain by a low-Q asthenosphere with Q_μ of 60-100. The lateral variation of the upper-mantle Q_μ perturbation appears to correlate with the lateral variation in the inverted shear-velocity perturbation.

15. SUBJECT TERMS
Seismology, seismic monitoring, earthquake location

16. SECURITY CLASSIFICATION OF: Unclassified			17. LIMITATION OF ABSTRACT	18. NUMBER OF PAGES	19a. NAME OF RESPONSIBLE PERSON Robert J. Raistrick
a. REPORT Unclassified	**b. ABSTRACT** Unclassified	**c. THIS PAGE** Unclassified	SAR		**19b. TELEPHONE NUMBER** *(include area code)* 781-377-3726

Standard Form 298 (Rev. 8-98)
Prescribed by ANSI Std. 239.18

Table of Contents

Foreword

The objective of this research is to map lateral variations of regional wave Q in eastern Eurasia using data from various sources, including the 36 new CNDSN stations in China. The seismic waves utilized include high-frequency regional phases *Lg, Pg, Pn*, and *Sn*, as well as long-period Rayleigh waves. The project was initiated by Dr. Jiakiang Xie, who completed much of the high-frequency regional wave analysis in the first two years of the project. Following Dr. Xie's departure for a position at AFRL, the project was continued at LDEO by co-PI's Dr. James Gaherty and Dr. Arthur Lerner-Lam. As a result, this final report consists of three appendices, each representing a distinct phase of the project.

Appendix A.
Tomographic regionalization of crustal Lg Q in eastern Eurasia
J. Xie, Z. Wu, R. Liu, D. Schaff, Y. Liu, and J. Liang

Tomographic regionalization of crustal Lg Q in eastern Eurasia

J. Xie,[1] Z. Wu,[2] R. Liu,[2] D. Schaff,[1] Y. Liu,[3] and J. Liang[2]

[1]   We measure Q of crustal Lg waves in eastern Eurasia using the reliable two-station methods. More than 5,000 spectral ratios are collected over 594 interstation paths, and are used to determine values of Lg Q_0 and η (Q at 1 Hz and its frequency dependence) over these paths. These values are used to derive tomographic models of laterally varying Q_0 and η with resolutions between 4 and 10°. The Q_0 model contains values that vary between 100 and 900. Q_0 are the lowest in the Tibetan plateau, increase to moderate levels towards the east and north, and reach maxima in the Siberian and eastern Europe Cratons. Q_0 values correlate well with regional tectonics. Most η values are between −0.14 and 0.50, with a mean of 0.18. These values are lower than those obtained previously using either an Lg coda Q method, or a method of simultaneous inversion of source spectra and Q. **Citation:** Xie, J., Z. Wu, R. Liu, D. Schaff, Y. Liu, and J. Liang (2006), Tomographic regionalization of crustal Lg Q in eastern Eurasia, *Geophys. Res. Lett.*, *33*, L03315, doi:10.1029/2005GL024410.

1.   Introduction

[2]   The Lg is typically the most prominent short period seismic phase observed over continental paths at distances greater than 200 km. Lg can be treated as a sum of higher mode surface waves, or multiple supercritically reflected S waves in the crust. The quality factor (Q) of Lg closely resembles the crustal average of shear wave Q. The Lg Q is known to be highly variable, by up to an order of magnitude, across major continents [e.g., *Xie and Mitchell*, 1990; *Xie et al.*, 2004]. Such large variations are caused by the fact that Q is strongly affected by crustal properties such as fluid contents and temperature, both of which can vary significantly from one region to another [*Mitchell et al.*, 1997]. Reliable measurements of Lg Q are difficult because the Lg amplitudes are affected by complications of source spectra and 3D velocity structures whose effects are difficult to fully account for, resulting in errors in Q measurement. Assuming that the long-duration coda of Lg is composed of singly scattered Lg by crustal heterogeneities, one can measure Lg coda Q using individual seismograms [*Xie and Mitchell*, 1990; *Mitchell et al.*, 1997]. The Lg coda Q should grossly approximate the Lg Q in the areas sampled by the scattered waves.

[3]   Among methods of measuring Q using direct Lg waves [e.g., *Xie et al.*, 1996; *Phillips and Hartse*, 2002], the standard two-station method has the advantage in that it allows the source spectra to be canceled in Q measurements. The reversed two station method [*Chun et al.*, 1987] further allows the cancellation of site responses. These methods, while being the most reliable, require strict recording geometries and hence dense station and event coverages.

[4]   The eastern part of the Eurasian continent that includes regions in and around China has a complex tectonic history. Currently the collision between the Indian and Eurasian plates to the southwest results in the uplifting of the Tibetan plateau. The extension along the east coast of China may be related to the underthrusting of the Pacific plate from the east. These collision and underthrusting processes serve as the primary driving forces of the current motions and deformations of a collage of blocks with diverse histories of evolution. Timing of the last significant tectonic activity that modified the crustal blocks ranges between Paleozoic and current. *Mitchell et al.* [1997] found the Lg coda Q values throughout Eurasia tend to correlate with the time that has elapsed since the last major tectonic activity. In the past decades there has been a steady accumulation of digital Lg waveforms from eastern Eurasia brought by the installation of various broad band seismic networks and the high seismicity. In this paper we report a tomographic regionalization of Lg Q in the region, obtained by applying the two station methods to more than 5,000 recently collected Lg spectral ratios.

2.   Data and Method of Q Measurement

[5]   One hundred and sixty two broad-band seismic stations are used in this study. The network affiliations include the Global Seismic Network (GSN) and various national or portable networks such as the Chinese National Digital Seismic Network (CNDSN), the Kyrghistan and Kazakhstan seismic networks, and the three passive networks deployed in the Tibetan Plateau [*Xie et al.*, 2004]. Vertical component Lg waveforms from 186 events between 1988 and 2004 are retrieved from Data Management Centers of Incorporated Research Institution of Seismology (IRIS) and CNDSN. Most events are moderately sized (with magnitudes clustered around 5.5). Fourier spectra of Lg are obtained using a well-established procedure to deal with noise and wave dispersion [*Xie et al.*, 1996, 2004]. More than 6,000 Lg spectra are collected. From these, 5,787 pairs of spectra are selected from two stations that are (1) aligned approximately with the source, (2) separated far enough (>250 km), permitting the use of the standard two-station method for Lg Q measurement [cf. *Xie et al.*, 2004,

---

[1]Lamont Doherty Earth Observatory, Columbia University, Palisades, New York, USA.
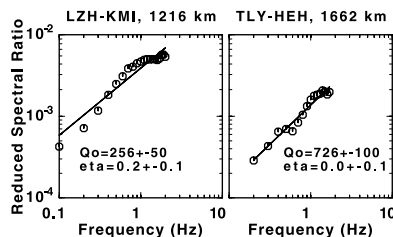[2]Institute of Geophysics, China Earthquake Administration, Beijing, China.
[3]Department of Geology and Geophysics, University of Wisconsin-Madison, Madison, Wisconsin, USA.
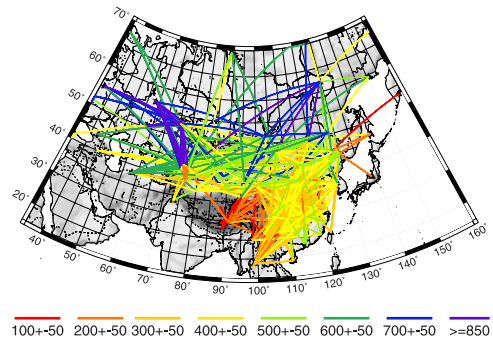
Figure 4]. About a quarter of these spectral pairs further satisfy the criterion of the reversed two-station, two-event condition (i.e., the sources that generated the ratios are located on the opposite azimuths viewed from the stations [c.f. *Chun et al.*, 1987, Figure 4]), permitting estimation of both inter-station Q free of site responses, and ratios of site responses [*Chun et al.*, 1987]. By examining the latter ratios a few stations are found to have non-unity site responses and/or erroneously documented instrument responses at levels higher than about 2. These stations are screened out in the subsequent analysis. This results in 5,265 useful spectral ratios that collectively sample 594 inter-station paths. Assuming that the Lg Q follow the power-law frequency dependence ($Q = Q_0 f^\eta$ where Q_0 is Q at 1 Hz and η is the frequency dependence), the inter-station Q_0 and η can be estimated using the following concise relationship (c.f. equations (2) through (4) of *Xie et al.* [2004]):

$$\ln\left\{\frac{V_{Lg}}{\pi\Delta_{i,j}}\ln\left[\frac{\Delta_i^{1/2}}{\Delta_j^{1/2}}\times\frac{A_i(f)}{A_j(f)}\right]\right\} = (1-\eta)\ln f - \ln Q_0, \qquad (1)$$

where V_{Lg} is the typical Lg group velocity of 3.5 km/s, Δ_i and Δ_j are the epicentral distances to the two aligned stations where Lg spectra $A_i(f)$ and $A_j(f)$ are collected, $\Delta_{i,j}$ is the interstation distance. In the above equations the left hand quantity is calculable from the observed spectral ratios ($A_i(f)/A_j(f)$)) and can be averaged over repeating two-station paths to provide stable estimate of Q_0 and η by a linear regression. We shall denote this quantity as "reduced spectral ratio." Average reduced spectral ratios are calculated over the 594 paths to estimate interstation Lg Q_0 and η. Typically, the lowest frequencies that yield usable reduced spectral ratios are between 0.1 and 0.3 Hz. The highest usable frequencies are primarily controlled by the signal/noise ratio threshold of 2 used in this study, and typically vary between about 1 and 2.5 Hz. Figures 1 and S1

Figure 2. Map showing two-station paths used in this study, with colors indicating the values of Q_0 estimated for the paths. An enlarged version of this map is shown in Figure S2 in the supplemental material.

in the supplemental material[1] show examples of reduced spectral ratios and the best fit Q models.
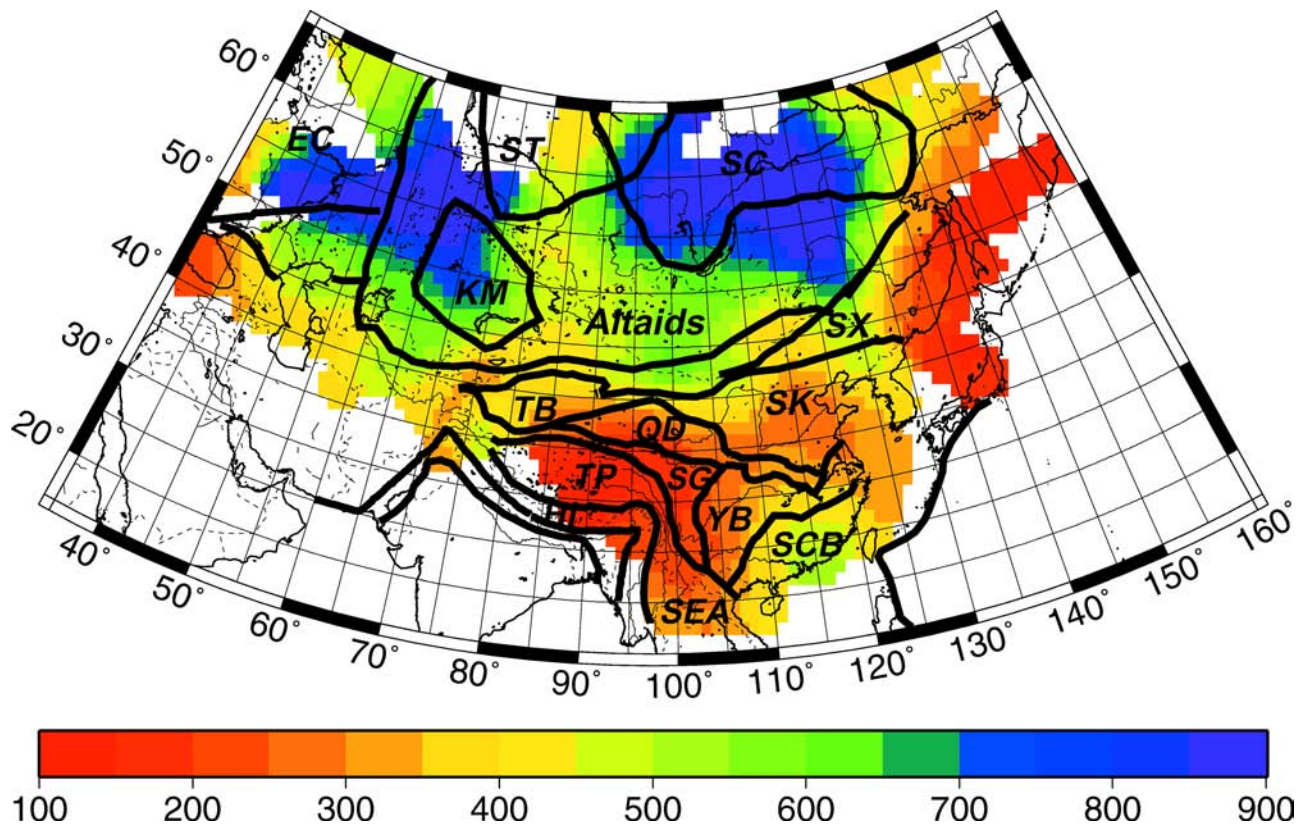
3. Result of Q Tomography

[6] Figures 2 and S2 show the 594 two-station paths with colors indicating the values of the Q_0 measurements. These values tend to be coherent on a large scale and are input to a tomographic back-projection algorithm to invert for the lateral variations in Q_0. The back-projection algorithm is a well established, iterative algorithm that reduces the model mistfit (residual) by updating Q_0 models along one path at a time (for more details, see *Xie and Mitchell* [1990] and *Xie et al.* [2004]). To parameterize the spatially varying Q_0, the study area is divided into about 2,300 cells with constant Q_0 values and a size of 2 by 2°. Figure 3 shows the resulting Q_0 model. The errors and resolution associated with the model are estimated using the algorithm of *Xie and Mitchell* [1990] and *Xie et al.* [2004]. Estimated random errors for the Q_0 model in Figure 3 are typically about 10–15%. The resolution, as measured by the point spreading functions, varies between about 4° in eastern China and about 10° in higher latitudes ($\geq$55°N).

[7] The most striking low Q_0 region in Figure 3 is that in and around the Tibetan Plateau where Q_0 is between about 100 and 200. Toward the east, Q_0 increases to about 300 in the Songpan-Ganzi Belt and Qaidam Basin, and to 300–550 in the Yangzi and south China blocks. To the north of these regions there is a band of moderate Q_0 regions (300–450) that covers the Tarim Block, the Ordos and the Sino-Korean Platforms. To the north of this band Q_0 increases with increasing latitude in the Altaids, to between about 400 and 600. Much of the Kazak Massif contains Q_0 values that are greater than 600. Variations of Q_0 in the northernmost subregions can be resolved only at scales of about 10° due to sparse ray coverage, with two broad regions of high Q_0 values between about 700 and 900 in the Siberian and Eastern Europe Cratons. Between these regions lies the Siberian Trap, a province that was affected by wide-spread volcanism and rifting in the late Paleozoic-Mesozoic time. Values of Q_0 in the Trap are between about 400 and 500,

Figure 1. Examples of average inter-station reduced spectral ratios (circles) and the best fit Lg Q models (lines, see equation (1)). Station codes, interstation distances and the estimated Q_0, η values are written in the panels. Left panel shows the average ratio over an inter-station path in southwest China, with sources located in the same direction, so the standard two-station method [e.g., *Xie et al.*, 2004] is used. Right panel shows the average ratio that samples an inter-station path mostly located in eastern Siberia, from sources located in opposite directions, so the method of *Chun et al.* [1987] is used.

Figure 3. Lg Q_0 map for eastern Eurasia obtained in this study, and simplified tectonic boundaries [e.g., *Mitchell et al.*, 1997; *Hearn et al.*, 2004; *Liang et al.*, 2004]. Abbreviations are: Tibetan Plateau (TP), Tarim Block (TB), Himalayas (HI), Songpan-Ganzi Belt (SG), Southeast Asia subplate (SEA), Yangtze block (YB), South China Block (SCB), Sino-Korean block (SK), Suolun-Xiamulun block (SX), Kazak Massif (KM), Siberia Craton (SC), Siberia Trap (ST) and Eastern Europe Craton (EC). The Ordos block is centered at about 117°E and 37.5°N [e.g., *Liang et al.*, 2004] and is merged into the SK for simplicity. Note the maximum latitude plotted is 5° less than in Figure 2.

relatively lower than in the Cratons. In general, Lg Q_0 values in Figure 3 exhibit a good correlation with the time since the last major tectonic events that modified the blocks, as found by *Mitchell et al.* [1997] for Lg coda Q_0 values. The variations of Lg Q_0 in Figure 3 in the southern and eastern portions are more drastic than those of Lg coda Q_0 shown in Plate 1 of *Mitchell et al.* [1997]. This indicates a higher resolution of the Lg Q model than the Lg coda Q model, which is expected since the Lg coda is composed of scattered Lg waves that sample elliptical areas rather than great-circles. Lateral variations in Lg coda Q_0 is inherently smeared out by this elliptical sampling pattern.

[8] The frequency dependence (η) values are measured using the slope of the linear regression to the reduced spectral ratios (equation (1); Figure 1 and Figure S1). In theory fitting the slope $(1 - η)$ is more unstable than fitting the intercept $(ln\ Q_0)$ when the data (reduced spectral ratios) are repeatedly sampled in a narrow range of $ln\ f$ near zero. In practice, *Xie et al.* [2004] state that to obtain stable measurements of η, a wide f range between about 0.1 and a few Hz is desirable. Unfortunately, many spectral ratios used in this study are only available in a relatively narrow frequency range between about 0.1 and 1 Hz owing to the rapid loss of high frequency signals at the more distant stations. We are therefore less confident at the measured η values for many individual paths. We examine the gross

distribution of the 594 η measurements by calculating their mean and standard deviation, which are 0.18 and 0.32, respectively. Therefore most η values are between −0.14 and 0.50. The mean η of 0.18 is lower than the mean η values of 0.4−0.5 obtained using Lg coda [*Mitchell et al.*, 1997] or a method of simultaneous inversion of source
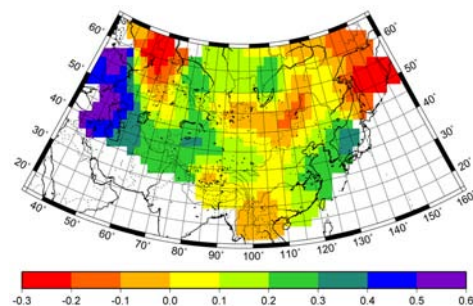
Figure 4. Map of power-law frequency dependence (η) obtained in this study. The cell size used in the inversion is 4 by 4° and twice as large as that used in Q_0 inversion (Figure 3). The larger size is used to avoid spurious oscillations of η caused by its measurement instability. An enlarged version of this map is shown in Figure S3 in the supplemental material.

spectra and Lg Q [*Xie et al.*, 1996]. This discrepancy in measured η values may result from systematic bias in the different measurement methods, each is based on specific assumptions. The Lg coda Q method assumes a single, frequency independent scattering process. The simultaneous inversion of source spectra and Q assumes an idealized, omega-squared source model. The two-station method assumes nothing about Lg scattering or source model, but has a strict requirement of recording geometry which often leads to a large epicentral distance (>1500 km) of the more distant station. The assumptions of Lg scattering or omega-squared source model may not be perfectly valid, or η could tend to decrease with recording distance in addition to varying laterally [*Xie et al.*, 1996]. Assuming that the distance dependence is not the case and η values measured in this study are not grossly biased, we may map the lateral variation of η spatially which results in broad regions with low η values (between -0.15 and 0.25) throughout the interior of the study area (Figures 4 and S3). Contrary to the similarity in Q_0 models obtained using Lg (this study) and Lg coda [*Mitchell et al.*, 1997], the η model in Figures 4 and S3 tends to be significantly lower than those in *Mitchell et al.* [1997].

4. Discussion

[9] Lateral variations of Lg Q at 1 Hz obtained in this study generally correlate with time since the last major tectonic event that modified the crustal Q structure. This correlation is similar to that found in a previous study of Lg coda Q [*Mitchell et al.*, 1997]. Values of power-law frequency dependence (η) of Lg Q measured in this study are systematically lower then those obtained previously using Lg coda, or using a method of simultaneous inversion of Lg source spectra and path Q. This discrepancy may be caused by break-downs of the stochastic Lg scattering or source models assumed by the previous methods, or an inherent distance-dependence of η caused by a distance-evolution of the Lg modal composition [*Xie et al.*, 1996]. Resolving this discrepancy is important because path-

corrections at high frequencies are critically dependent on accurate η values, and because inference of layered crustal Q structures and their causes can be made using η values [*Mitchell et al.*, 1997; *Xie et al.*, 2004]. Future research using data with high signal/noise ratios in a wider frequency range should enable us to determine η values reliably, and to explore the cause of the η discrepancy.

References

Chun, K. Y., G. F. West, R. J. Kokoski, and C. Samson (1987), A novel technique for measuring Lg attenuation - Results from eastern Canada between 1-Hz to 10-Hz, *Bull. Seismol. Soc. Am.*, *77*, 398–419.
Hearn, T. M., S. Y. Wang, J. F. Ni, Z. H. Xu, Y. X. Yu, and X. D. Zhang (2004), Uppermost mantle velocities beneath China and surrounding regions, *J. Geophys. Res.*, *109*, B11301, doi:10.1029/2003JB002874.
Liang, C., X. Song, and J. Huang (2004), Tomographic inversion of Pn travel times in China, *J. Geophys. Res.*, *109*, B11304, doi:10.1029/2003JB002789.
Mitchell, B. J., Y. Pan, J. Xie, and L. Cong (1997), Lg coda Q variation across Eurasia and its relation to crustal evolution, *J. Geophys. Res.*, *102*, 22,767–22,780.
Phillips, W. S., and H. E. Hartse (2002), Regional path calibration using multiple-station amplitude tomography, *Seismol. Res. Lett.*, *73*, 228.
Xie, J., and B. J. Mitchell (1990), A back projection method for imaging large scale lateral variation in Lg coda Q with application to continental Africa, *Geophys. J.*, *100*, 161–181.
Xie, J., L. Cong, and B. J. Mitchell (1996), Spectral characteristics of the excitation and propagation of Lg from underground nuclear explosions in Central Asia, *J. Geophys. Res.*, *101*, 5813–5822.
Xie, J., R. Gok, J. Ni, and Y. Aoki (2004), Lateral variations of crustal seismic attenuation along the INDEPTH Profiles in Tibet from Lg Q inversion, *J. Geophys. Res.*, *109*, B10308, doi:10.1029/2004JB002988.

————————————

J. Liang, R. Liu, and Z. Wu, Institute of Geophysics, China Earthquake Administration, No, 5 Mingzuxueyuan Nanlu, Beijing 100081, China. (wuzhl@gscas.ac.cn)

Y. Liu, Department of Geology and Geophysics, University of Wisconsin-Madison, 1215 W. Dayton St., Madison, WI 53706, USA. (yunfengl@geology.wisc.edu)

D. Schaff and J. Xie, Lamont Doherty Earth Observatory, Columbia University, 61 Route 9W, Palisades, NY 10964, USA. (xie@ldeo.columbia.edu)

Appendix B.
Pn attenuation beneath the Tibetan Plateau
J. Xie

Pn attenuation beneath the Tibetan Plateau

Jiakang Xie

Abstract Pn spectra are collected from three PASSCAL seismic experiments in the Tibetan Plateau (TP) over four path groups to study Pn attenuation. The first and second path groups run southward from the Lop Nor Test Site (LTS) to stations in north and south central Tibet. The third and fourth path groups form two NNE-oriented profiles in the eastern TP. Events recorded by the first 2 path groups are also recorded over central Asian paths running westerly from the LTS to the Khyrghistan network (KNET). A comparison of Pn spectra from these events reveal that mantle lid under north central TP attenuates Pn more severely than under central Asia. Apparent Q_0 and η (Pn Q at 1 Hz and its frequency dependence) are estimated with a simplified geometrical spreading (G.S.T.) of $\Delta^{-1.3}$. Over path group 1 that heavily samples northern TP, Q_0 and η are estimated to be 183±33 and 0.3±0.1. Over path groups 2 and 3 that sample either a mixture of northern and southern Tibet or eastern Tibet, Q_0 and η are between about 250-270 and 0.0-0.1, respectively. Over the fourth path group that sample the easternmost TP the respective estimates are 374±51 and 0.3±0.1, similar to the estimates of 364 and 0.5 for central Asian paths from LTS to KNET. A comparison of total Pn attenuations that include effects of both G.S.T. and Q in continental regions show that they are similar in relatively stable regions of central Asia, Scandinavia and Canadian shield. Within the TP, Pn attenuation is the highest under north central Tibet, and decreases toward south and east. In easternmost Tibet Pn attenuation becomes similar to those in stable regions. Lateral variation of Pn attenuation inversely correlates with that of the Pn velocity. Possible causes of this variation include (1) a thermally driven mantle Q_p, and (2) region-specific velocity structures, which may be characterized by different lid gradients, and density and aspect ratios of 3D scatterers in the vicinity of the Moho.
Abbreviated title: Pn attenuation in Tibet

Introduction

Pn is the first arriving high-frequency seismic phase at regional distances between about 2-15°. It is an important phase to be used in location, identification and size-estimation of seismic events, and in inferring the velocity and attenuation structures of the Earth's uppermost mantle. At close distances Pn is much like a mantle head wave, which evolves into mantle turning waves with increasing distance (*e.g.,* Sereno and Given, 1990). This peculiar wave evolution causes the features of Pn, such as its ray geometry, travel time and amplitude to vary with distance in manners that are highly dependent on the velocity gradient in the mantle lid. Simplifications to these variations are typically introduced when Pn data is used to study lid structures. Pn arrival times have been extensively used to study the lateral variations of compressional wave velocity (v_p) in the lid (e.g., Hearn et al., 1986). Most studies have ignored effects of the mantle velocity gradient and treated Pn as a pure head wave at all distances. A few studies, such as Zhao and Xie (1993) and Hearn et al. (2004), accommodated the first-order effect of velocity

gradient and obtained v_p models that vary both laterally and vertically in the mantle lid.

Few studies have been conducted to use Pn amplitude to estimate its attenuation, or Q. A fundamental difficulty in such studies is caused by the lack of knowledge of the geometrical spreading term (G.S.T.), which describes the Pn amplitude fall-off with distance owing to the wavefront expansion in the mantle lid. The Pn G.S.T. is very sensitive to details of the lid velocity structure. Sereno and Given (1990), Xie (1996), Lay et al. (2006) and Yang et al. (2007) estimated the G.S.T. of Pn for Scandinavia, central Asia and China using synthetic seismograms calculated for various 1D velocity models. They found even for these simplified models the G.S.T. varied with distance and frequency in rather complex manners. In the real 3D Earth structure, even more complications are expected. For example, scattering and multiple bouncing (whispering-gallery) processes may affect the Pn wavetrain (e.g., Menke and Richards, 1980, 1983; Kvaerna and Doornbos, 1991; Ryberg et al., 1995; Morozov and Smithson, 2000; Nowack and Stacey, 2002; Nielsen and Thybo, 2003). To tackle the uncertainty in G.S.T., different parameterizations have been used in studies of Pn amplitude attenuation. On the basis of coarse fits of synthetic seismograms, Sereno et al. (1988) and Xie and Patton (1999) assumed a simplified, frequency independent G.S.T. of $\Delta^{-1.3}$ and estimated models of Pn Q ($Q(f)$) in Scandinavia and central Asia. They assumed a power-law frequency dependence of Pn Q,

$$Q(f) = Q_0 f^\eta \quad , \tag{1}$$

where Q_0 and η are Pn Q at 1 Hz and its frequency dependence, respectively. They obtained similar Q_0 values of 325 and 364, and η values of ~0.5 for the two regions. Zhu et al. (1991) simultaneously estimated a frequency-dependent G.S.T. and $Q(f)$ for Canadian shield. Other authors such as Tinker and Wallace (1997), who studied Pn attenuation at near-regional distances within about 350 km, simply parameterized Pn attenuation by a single G.S.T. without Q.

The mantle lid under the Tibetan plateau (TP) is known to have highly laterally variable P wave velocities (v_p). Zhao and Xie (1993), McNamara et al. (1997) and Hearn et al. (2002) used Pn arrival time data to invert for the laterally varying v_p models. Their v_p models contain grossly similar features such as a zone of low v_p under northern TP, and high v_p under much of southern TP. Ni and Barazangi (1983) and McNamara et al. (1995) also found that the Sn wave, which is the shear wave that traverses the mantle lid similarly to Pn, seemed to suffer abnormally high attenuation under northern TP. These findings are used to infer that the mantle lid is hot and partially molten under a broad region in northern TP, and cold under southern TP. Results of Pn and Sn studies contributed to the development of a geodynamic model in which the Indian lithosphere underthrusts in southern TP (Nelson et al., 1996), and subducts into the mantle further south, along the latitude of ~32°N (Tilmann et al., 2003).

Measurements of Sn attenuation under TP is limited to a qualitative comparison of the relative amplitude of Sn to that of P coda. By contrast, the amplitude spectra of the Pn wavetrain can be quantitatively calculated at the distances where Pn is the first arrival. In this paper we present analyses of the attenuation of Pn spectra recorded during three PASSCAL experiments in TP. We first analyze Pn spectra from three events that occurred in 1994 or 1999 in the Lop Nop Nor Test Site (LTS) of eastern Tarim Basin, which are simultaneously recorded by the INDEPTH (International Deep Profiling of Tibet and the Himalaya) II or III stations to the south crossing the TP, and Khyrghistan

network (KNET) to the west crossing eastern Tienshan. A comparison of raw Pn spectra recorded by the INDEPTH and KNET stations provides direct evidence that the mantle lid under the TP is more attenuative than that under eastern Tienshan. We then quantify the Pn attenuation along paths to INDEPTH networks by estimating apparent Pn Q under a simplified G.S.T. and omega-squared source models. This is followed by two-station measurements of apparent Pn Q along two PASSCAL profiles in eastern Tibet, deployed during the 1991-1992 Tibetan Plateau experiment. We report a spatial trend for the apparent Pn Q at 1 Hz (Q_0) to be low in north central TP, and to increase both southward and eastward. This trend correlates with the spatial variation of Pn velocity measured in previous studies. Finally we compare the total Pn attenuations reported for various continental regions in the world, by taking into account both the G.S.T. and Q model. We find that in the Canadian and Scandinavian shields, central Asia, and easternmost TP where Pn velocity is high (≥ 8.0 km/s), the total Pn attenuations are similar to one another and much weaker than that under the northern TP. We infer possible causes of the regional variation of Pn attenuation, including variations in either a temperature-sensitive lid Q_p and/or in fine-scale velocity structures in the vicinity of the Moho.

Data Processing

Figure 1 shows all seismic stations in Tibet deployed during the three PASSCAL experiments. The 1991-1992 Sino-US Tibetan Plateau experiment consisted of 11 broad-band stations that were deployed between July, 1991 and July, 1992 (Owens et al., 1993) in the eastern part of the plateau. The INDEPTH II experiment was conducted in southern Tibet between May and October, 1994 (Nelson et al., 1996) with 15 broad-band or short-period stations deployed along an NNE-oriented profile. The INDEPTH III experiment was conducted in central Tibet between July, 1998 and June, 1999. Forty-seven broad or intermediate band and 15 short-period stations were deployed along a profile across the Banggong-Nujiang Suture (BNS) in a NNW direction (Figure 1; also c.f. Rapine et al., 2003). Stations in all three experiments are three-component, with sampling rates of 20 s^{-1} or higher. Figure 1 also shows regional events used in this study. Figure 2 shows an example of the record sections containing Pn.

To obtain stable estimates of Pn amplitude spectra, a finite-length wavetrain that included Pn and its coda was previously used by Sereno et al. (1988), Zhu et al. (1991) and Xie and Patton (1999). In this study we follow the procedure by these authors to compute average spectra of Pn and Pn coda, using spectra from a series of overlapping windows applied to the vertical-component seismograms. These windows have a constant length of 4.5 s, a 20% taper and 50% overlap. Only spectra with signal to noise ratios larger than 2 are used. The maximum number of the windows for a given seismogram is determined by the following criteria: (a) the total length of Pn wavetrain sampled does not exceed 12.5 s (i.e., the maximum window number is 5), (b) at closer distances ($\Delta <$ 1000 km) the last window does not include signals with group velocities slower than 6.6 km/s so that the crustal Pg wave is excluded; and (c) at large distances ($\Delta \sim 1500$ km) the last window does not include the possible reflections from the 440 km and 660 km discontinuities, previously observed in Tibet (8301 Program Group, 1988). Figure 3 shows an example of the windows used, and the resulting individual and average Fourier spectra of the Pn wavetrain. The effect of ambient noise is reduced by subtracting the signal power by the noise power. Instrument responses are then removed. We shall refer to the

average spectra thus calculated for the Pn wavetrain as "Pn spectra" in the rest of the paper.

Features of Pn Spectra from Events in the Lop Nor Test Site

Spectra from the 1994 Explosions

During the INDEPTH II experiment, two underground nuclear explosions occurred in the LTS of eastern Tarim Basin (Figure 1). Pn wavetrains were recorded by all 12 operational INDEPTH stations for the October 7 (m_b=5.9) explosion (Figure 2), and by 7 stations for the June 10 (m_b=5.7) explosion. Pn spectra from both explosions were also recorded by the Khyrghistan network (KNET) to the west (Figure 1), and studied by Xie and Patton (1999). The paths to the KNET stations traverse to the eastern Tienshan. In comparison, the paths to the INDEPTH II network run southward and sample the TP. Both groups of paths have similar, far-regional distances between about 1050 and 1550 km (Figure 1). Any anisotropic Pn radiation patterns are expected to be minimal. There-fore we may directly compare the Pn spectra to see the gross attenuation effect of the mantle lid under Tienshan and the Tibetan Plateau. The top two rows of Figure 4 show the Pn ground displacement spectra from both explosions, scaled by $\Delta^{1.3}$ to reduce the effects of G.S.T.

A prominent feature of the Pn spectral amplitudes from both explosions is their variability within the networks, particularly within the KNET. Both networks have aper-tures of less than about 350 km compared to the average path lengths of > 1050 km. Yet the sample standard deviation is typically at the level of ~60% of the averaged spectra for the KNET stations, and range between ~60% (at frequencies < 1 Hz) and ~30% (at fre-quencies > 1 Hz) for the INDEPTH stations. For both networks the amplitude variations are not monotonic with distance, so path attenuation from finite Q is not the primary cause of these variations. Xie (1996) and Xie and Patton (1999) concluded that the most likely cause for the drastic Pn amplitude variations across the KNET is a laterally varying Moho topography that likely occurs along the Tienshan range. Xie (1996, 2003) con-ducted ray tracings in 2D velocity models for Central Asia in and around the Tienshan region to demonstrate the potential effect of Moho topography. Significant amplitude variations of Pn over short distance ranges seem to be common in other mountainous regions in the world (e.g., Tinker and Wallace, 1997). The use of a finite duration wave train to calculate Pn spectra has not sufficiently suppressed its variability. Therefore to study the gross effect of whole-path attenuations, we take the network average of Pn spectra, as shown in the right columns of Figure 4.

The network-averaged Pn spectra from the well recorded, October 7 explosion (top right panel of Figure 4) start at similar levels at similar distances for KNET and INDEPTH II at the lowest frequency (~0.4 Hz). With increasing frequency the average spectrum from the INDEPTH II network rapidly falls below that from the KNET. At ~1 Hz the separation between the two spectra reaches a factor of 4. At higher frequencies the separation increases monotonically with frequency and overwhelms the variabilities within the networks as measured by the standard deviations. At 4 Hz (the highest fre-quency available for INDEPTH spectra), the separation reaches a factor of ~35. Network averaged spectra from the June 10 explosion (right panel of row 2 of Figure 4) have a

10

similar, frequency-dependent separation, although the smaller event size causes both fewer recordings and narrower recording bands. Since the recording distances to KNET and INDEPTH networks are similar, the frequency dependent separations between the network-averaged Pn spectra from both explosions mean that Pn attenuation under the Tibetan plateau and Tienshan is similar at low frequencies (~0.4 Hz), but becomes increasingly different with increasing frequency.

Spectra from the 1999 Earthquake

Event "99.030" in Figure 1 is an m_b=5.9 earthquake on January 30, 1999, which is located nearby the 1994 explosions. The event is simultaneously recorded by 10 KNET and 38 INDEPTH III stations. Of the latter, 35 are deployed along a main profile that crosses the BNS, and 3 are deployed on the BNS but outside the main profile (Figures 1 and 5). Pn velocity analyses reveal that the BNS is an approximate boundary separating regions of abnormally slow and fast mantle lid velocities (Zhao and Xie, 1993; McNamara et al., 1997; Hearn et al., 2002; Xie, 2003). So in this study we have divided the INDEPTH III stations into two groups. Group 1 (denoted as III-1) contains 15 stations south of the BNS and group 2 (denoted as III-2) contains 23 stations north of, and on, the BNS (Figure 5). Rows 3 and 4 of Figure 4 show the Pn spectra from KNET and the two groups of INDEPTH III stations. As in the case of Pn spectra from the explosions (top two rows in Figure 4), the spectra from the earthquake (bottom two rows) also exhibit substantial variations within each network. The averages of Pn spectra from KNET and INDEPTH III stations also exhibit a frequency-dependent separation, indicating more severe attenuation of the Tibetan mantle lid at higher frequencies. There are also notable differences between explosion and earthquake spectra. Whereas the explosion spectra contain spectral overshoot effects near the source corner frequencies (e.g., above 1 Hz for the October 7 explosion), the earthquake spectra (bottom rows) exhibit no overshoot and decay more gently (see Xie and Patton, 1999, for details).

Stochastic Modeling of Pn Spectra

To quantitatively estimate Pn Q and source spectra, we use the stochastic modeling of Pn spectra used by Sereno et al. (1988) and adapted by Xie and Patton (1999). For convenience we briefly summarize the modeling here. We assume that Pn spectra, $A(f)$, can be modeled by

$$A(f) = S(f)R(\theta)G(\Delta)\exp\left(-\frac{\pi f \Delta}{VQ(f)}\right)X(f) \ , \qquad (2)$$

where θ, Δ, V are the azimuth, distance and Pn group velocity, respectively. $Q(f)$ is Pn Q (equation (1)). $R(\theta)$ is the source radiation pattern. $X(f)$ is an error term that represents systematic errors such as a non-unity site response, and random errors caused by amplitude fluctuation. $S(f)$ is the Pn source spectrum, which is given by the Brune's model and Modified Mueller-Murphy (MMM) model for earthquakes and explosions, respectively (equation (2) of Xie and Patton, 1999). Both models have f^{-2} asymptotic decays at high-frequencies, and are grossly characterized by a seismic moment (M_0) and corner frequency (f_c). The MMM model for explosions also has a spectral overshoot controlled

11

by a parameter β, which is set as 1.0 by Xie and Patton (1999). In equation (2), $G(\Delta)$ is the geometrical spreading term (G.S.T.) and takes the form,

$$G(\Delta) = \Delta_0^{-1}(\Delta_0/\Delta)^m \tag{3}$$

where Δ_0 is a reference distance, and m is the decay rate of $A(f)$ at large distances $(\Delta > \Delta_0)$. As mentioned in the Introduction, a well known problem in modeling Pn is that the values of Δ_0 and m are uncertain because of the unknown details of the lid velocity structure. Based on theoretical and empirical considerations, Sereno *et al.*, (1988) used Δ_0 and m of 1 km and 1.3, respectively, for Scandinavia. Xie (1996) found that these values were also within the ranges obtained using synthetic Pn waveforms in various 1D velocity models for central Asia. Therefore Xie and Patton (1999) used these Δ_0 and m values to study Pn spectra from several nearly colocated explosions in the LTS, recorded by the KNET in the west, and the Kazakhstan network (KZNET) in the north. To obtain robust estimates of source and path parameters with a minimum trade-off among them, Xie and Patton first estimated source f_c values using the empirical Green's function method, and path-variable Pn Q using a two-station and a composite event method. These estimates were then input as a priori knowledge to an Bayesian inverse method to measure M_0 and refined f_c values for all explosions. The Pn Q values by Xie and Patton (1999) are apparent because of the specific G.S.T. used, but are robust because the multiple-event, multiple-constraints used. These values will be used as a priori knowledge in this study.

Estimates of Apparent Pn Q to Indepth Stations

The October 7 explosion was recorded by 8 KNET stations. The average Q_0 and η to these stations were estimated to be 381 and 0.4, respectively (Xie and Patton, 1999). We input these values to the Bayesian method to estimate source M_0, f_c and path-variable Q_0, η values to the INDEPTH II stations (Equation (2), also see equation (13) of Xie and Patton, 1999). Figure 6 (row 1) shows the fit of the resulting source spectral and path Q models to the observed spectra from the INDEPTH II network and KNET. The estimated M_0, f_c values are the same as those previously obtained by Xie and Patton (1999; 3.2×10^{15} Nm and 2.6 Hz, respectively). The estimated average Q_0 value to the INDEPTH II stations is 253±53, which is 30% lower than the value of 364 to all 12 KNET stations estimated by Xie and Patton (1999). The average η to INDEPTH II stations is 0.0±0.1, which is much lower than the average η of 0.5 estimated to the KNET stations. The June 10 explosion is relatively poorly recorded as mentioned in a previous section. We are not confident at estimating Q using that event.

Earthquake 99.030 was recorded by all 12 KNET stations and 38 INDEPTH III stations. We assume that for this earthquake the source radiation pattern ($R(\theta)$ in equation (2)) does not vary significantly to the former and latter stations. This assumption is justified quantitatively in the Appendix. The assumption allows us to use the average Q_0, η values to KNET estimated by Xie and Patton (1999; 364 and 0.5, respectively) as a priori information in the Bayesian inversion in the same way as we did for explosions. The resulting estimates of source M_0 and f_c values are 2.49×10^{16} Nm and 0.8 Hz, respectively. Our f_c estimate has an uncertainty of about 0.1 Hz and is very consistent with the estimated f_c range between 0.72 and 0.78 Hz for this event, obtained separately using an

empirical Green's function method by Dr. Mark Fisk (M. Fisk, written communication, September, 2006). The average Q_0 and η values to the southern station group, III-1, are estimated to be 255±48 and 0.1±0.1. These values are similar to those to the INDEPTH II stations estimated above. By contrast, the average Q_0 and η values to station group III-2, located to the north of BNS, are estimated to be 183±33 and 0.3±0.1, respectively.

The Q_0 and η estimates presented in this section are those along long paths from LTS and contain small crustal segments in both the source and receiver end, and short mantle segments in the Tarim Basin. The two-station method (Xie et al., 2004), when applicable, can minimize effects of both attenuation outside the networks and the source radiation. We attempted to use that method to estimate Pn Q along the INDEPTH profiles but obtained very unstable (negative) Q values. This is caused by the large variability of Pn spectral amplitudes within the INDEPTH II and III networks (Figure 4) which means errors ($X(f)$ in equation (2)) are large. Xie et al. (2004) pointed out that at a given frequency, the effect of error ($X(f)$) in Q estimates could be suppressed by using large measuring distances. Unfortunately the INDEPTH profiles are short (< 350 or 400 km; see Figure 1), resulting in small inter-station distances that are not adequate to suppress the large $X(f)$.

Apparent Pn Q along Passcal Profiles in Eastern Tibet

Stations deployed during the 1991-1992 Sino-US Tibetan Plateau experiment (Owens et al., 1993) recorded Pn spectra from four regional earthquakes (Figures 1 and 5) that are approximately in line with profiles SANG-TUNL and SANG/GANZ-MAQI in eastern Tibet. Inter-station distances along these profiles are generally large so the effect of the error term ($X(f)$) in two-station Q measurements should be reduced (last section). We use Pn spectra along these profiles to estimate spectral ratios from many pairs of two-stations. These ratios are then averaged along profiles SANG-TUNL, SANG/GANZ-MAQI and WNDO-TUNL to estimate Q_0 and η using equation (4) of Xie et al. (2004), replacing V_{Lg} by a Pn phase velocity of 8.0 km/s. Profile SANG/GANZ-MAQI is merged from two subprofiles SANG-MAQI and GANZ-MAQI. Profile WNDO-TUNL is actually the northern half of profile SANG-TUNL; it is used to see if Pn Q changes from south to north along profile SANG-TUNL that crosses the BNS. Figure 7 shows the stacked spectral ratios (SSRs) along the three profiles and the best fitting models of Q_0 and η. At most frequencies (> 0.7 Hz) the SSRs closely follow the straight lines representing the best fitting models. The SSRs at frequencies lower than 0.7 Hz are abnormally small along all profiles. These may be caused by a trend of increasing effects of modeling errors ($X(f)$) in Q estimates toward lower frequencies, as predicted by Xie et al. (2004). The Q_0 and η values estimated along profile SANG-TUNL are 278±23 and 0.1±0.1, respectively (Figure 7), similar to those estimated for paths from Lop Nor to the INDEPTH stations in southern Tibet (last section). There is no significant north-south change of Q_0 and η values along profile SANG-TUNL since the values estimated along its northern half (profile WNDO-TUNL) are 273±32 and 0.0±0.1 (Figure 7), virtually the same as those estimated along the entire profile. The Q_0 and η estimated along profile SANG/GANZ-MAQI, which is located in the easternmost TB, are about 374±57 and 0.3±0.1, similar to the values of 364 and 0.5 estimated for paths from the Lop Nor to KNET (Xie and Patton, 1999, also see the last section).

13

A Comparison of Pn Attenuation in Continental Regions

Figure 5 summarizes all apparent Q_0 and η values estimated in this study and Xie and Patton (1999) for regions in and around the Tibetan plateau and Tienshan. Paths from the LTS to north central Tibet are associated with the lowest Q_0 (~183). Higher Q_0 values are found along paths from LTS to south central Tibet, and along the two profiles in eastern Tibet. These Q_0 and η values allow us to compare Pn attenuation in the TP to those in other continental regions. As mentioned in the Introduction, there have only been few previous publications documenting Pn attenuation on continents at far-regional distances. The published Pn Q values are obtained using different G.S.T. (Sereno et al., 1988; Zhu et al., 1991; Xie and Patton, 1999). To compare them with those obtained in this study, we calculate models of total Pn attenuation in the frequency domain at a reference distance of 1200 km (Figure 8). The calculation simultaneously accounts for the G.S.T. used, and the estimated Pn Q. Pn attenuation models are similar for the relatively stable regions where mantle Pn velocities are higher than 8.0 km/s, including the Canadian shield, Scandinavia, central Asia and easternmost Tibet (omitted in Figure 8; see caption). This is so despite that the G.S.T. used for the Canadian Shield by Zhu et al. (1991) has a frequency-dependent form of $m=1.07+0.035f$, rather than $m=1.3$ used for other regions.

The lowest model (corresponding to the strongest Pn attenuation) in Figure 8 is that for paths from LTS to northern Tibet (model "N. TP"). At all frequencies the model is below those for the stable regions, but the differences are more drastic toward higher frequencies. At 4 Hz the differences are more than a factor of 100. The second lowest model in Figure 8 is Model C. TP. which at most frequencies is much below those for stable regions, while being somewhat higher than model N. TP. There are two possible causes for models N. T.P. and C. T.P. to be lower than models for stable regions. The first one is that the intrinsic Q_p under northern Tibet may be low. This cause is empirically supported by the monotonic increase of the differences between the Tibetan and other models with frequency in Figure 8. Such frequency content shift among seismic spectra is a typical indicator of a varying Q (e.g., Ruzaikin et al., 1977; Fan and Lay, 2002; Xie et al., 2002). A physical reasoning for this cause is based on the fact that intrinsic Q_p is known to be strongly dependent on temperature (e.g., Mitchell, 1995). As mentioned in the Introduction, analyses of lateral variations in Pn velocity have led to the inference that the temperature in the mantle lid under north central Tibet is abnormally high, likely reaching the solidus and causing partial melting. By contrast, the lid temperature beneath southern Tibet (south of the BNS in Figures 1 and 5) is abnormally low owing to the underthrusting Indian lithosphere. Since model N. TP most heavily samples the hot lid under north central Tibet, it is expected to be most affected by the low Q_p caused by high temperature there. Model C. T.P. is developed for paths from LTS to southern Tibet (Figure 5) and samples a mixture of the hot lid under north central Tibet and cold lid under southern Tibet, so the average Q_p is expected to be higher than that of model N. T.P., making model C. T.P. somewhat above N. T.P. These expected Q_p levels well explain why models N.T.P. and C.T.P. are the first and second lowest in Figure 8. The second possible cause for the T.P. models to be low is a regional variation of the near Moho-velocity structure. Studies using synthetic seismograms have shown that the Pn wavetrain may be composed of diving and whispering-gallery waves whose propagation efficiency, or G.S.T., may be sensitive to details of the velocity structure near the Moho

(Menke and Richards, 1980; 1983; Sereno and Given, 1990; Kvaerna and Doornbos, 1991). In particular, a positive lid velocity gradient may retain more Pn energy by refraction. Likewise an enhanced distribution of horizontally elongated scatterers in the mantle lid or lower crust may strengthen Pn by forward-scattering (e.g., Ryberg et al., 1995, Morozov and Smithson, 2000; Nowack and Stacey, 2002; Neilsen and Thybo, 2003). As will be elaborated below, we can not rule out this second cause because we fundamentally lack knowledge of detailed regional velocity structures involved.

Discussion

In this study we have measured apparent Pn Q with a simplified geometrical spreading term (G.S.T.) of $\Delta^{-1.3}$. That G.S.T. was used in the past in Scandinavia and central Asia (Sereno et al., 1990; Xie and Patton, 1999) and is within a range of G.S.T. obtained using synthetic Pn waveforms in various 1D velocity models for central Asia (Xie, 1996). We can not improve that G.S.T. using synthetic seismogram calculations because we do not have detailed knowledge of the velocity structure in the vicinity of the Moho. For example, previous Pn velocity models for the T.P. lack the resolution for inferring whether there is an abnormally negative sub-Moho gradient under north-central Tibet (e.g., 8301 Group, 1988; Zhao and Xie, 1993; McNamara et al., 1997). Inferring features of 3D scatterers, such as their density and aspect ratios that may strongly affect Pn G.S.T. (end of last section) would be even more difficult as it requires even higher resolution. Zhu et al. (1991) proposed to use the observed Pn spectral ratios to simultaneously fit a frequency-dependent G.S.T. and Pn Q model. A concern about that approach is that there is likely a trade-off between the estimated G.S.T. and Q (Sereno et al., 1990; Xie and Patton, 1999). To see if such trade-off exists in our dataset, we conduct numerical tests in which we fit two-station spectral ratios along the Passcal profiles in eastern Tibet by various combinations of G.S.T. and Q, and examine how much the resulting residuals vary. Figure 9 shows an example of such tests, in which stacked spectral ratios along profile SANG-TUNL are fit by the G.S.T. of $m = 1.07 + 0.0035 f$ estimated by Zhu et al. (1991), together with a Q_0 and η of 241 and 0.20. The residual of this new fit is 0.6646. In comparison, the residual obtained earlier using $m = 1.3$, $Q_0 = 278$ and $\eta = 0.1$ (top panel of Figure 7; replotted in Figure 9) is 0.6660. These two residuals differ by only 0.2%, suggesting a nearly complete trade-off between G.S.T. (m) and Q (Q_0 and η). Since we will unlikely be able to acquire precise knowledge of the Pn G.S.T. and its regional variations in the near future, the estimated Pn Q will be apparent Q which only approximates the true Q. Such apparent Q does not provide input for a precise estimate of lid temperature using a Q-T relationship (e.g., Mitchell, 1995). In the practical path corrections, total Pn attenuation that combines the effects of Pn Q and the respective G.S.T. should be used.

Conclusions

Pn attenuation is studied using data from three PASSCAL experiments in the Tibetan Plateau (TP), including the 1991-1992 Sino-US TP, the INDEPTH (International Deep Profiling of Tibet and the Himalaya) II and III experiments. Three seismic events in the Lop Nor Test Site (LTS) are simultaneously recorded by the INDEPTH II and III networks to the south and the Khyrghistan network (KNET) to the west, at similar far-regional distances ($\geq$ 1050 km). A comparison of the recorded Pn spectra yields direct

evidence that the mantle lid under the TB is more attenuative than that under central Asia at high frequencies (> 1 Hz). At 4 Hz, the difference in attenuations cause the INDEPTH spectra to be about a factor of 35 smaller than the KNET spectra.

Under a simplified Pn geometrical spreading of $\Delta^{-1.3}$, we measure Q_0 and η (apparent Pn Q at 1 Hz and its frequency dependence, respectively) along various path groups. For paths from LTS to northern Tibet we estimate Q_0, η to be 183±33 and 0.3±0.1, respectively. For paths to southern Tibet, and along a profile (SANG-TUNL) in eastern Tibet deployed during the 1991-1992 experiment, Q_0 increases to above 250, while η decreases to about 0.0-0.1. Along a profile in the easternmost Tibet (SANG/GANZ-MAQI), Q_0 increases further to 374±51, while η is 0.3±0.1. These values are similar to those of 364 and 0.5 measured along central Asian paths from LTS to KNET.

We define total Pn attenuation as the combined effect of geometrical spreading and finite Q and calculate it at a reference distance of 1200 km for various continental regions. In the stable regions of central Asia, Scandinavia and the Canadian shield where Pn velocity is higher than 8.0 km/s, Pn attenuation is similarly low. Among regions in and around the TP, Pn attenuation is the strongest under north central Tibet, and decreases toward the south and east. In the easternmost TP, Pn attenuation becomes as low as that in the stable regions. The spatial variation of Pn attenuation correlates inversely with that of Pn velocity. A probable cause of this phenomenon is that Pn attenuation is directly affected by the intrinsic Q_p in the mantle lid, where a variation in temperature causes both Q_p and v_p to vary. It is also possible that regional variations of velocity structure in the vicinity of the Moho, such as variations of lid gradient and/or density and aspect ratios of the 3D scatterers, also play a role in causing regionally variable Pn attenuation.

Acknowledgements

References

8301 Program Cooperation Group, (1988). Velocity structure of crust and upper mantle at the east margin of Tarim Basin and the east part of Qinghai-Tibet Plateau, in *Developments of the Research of Deep Structures of China's Continent*, Department of Scientific Programming and earthquake Monitoring, China Seismological Bureau, (*ed.*), Geology Publisher, Beijing, 89-96.

Fan, G.-W. and T. Lay (2002). Characteristics of Lg Attenuation in the Tibetan Plateau, *J. Geophys. Res.*, **107(10)**, ESE14, doi:10.1029/2001JB000804.

Hearn T.M. and R.W. Clayton (1986). Lateral velocity variations in southern-California . 2. Results for the lower crust from Pn waves, *Bull. Seism. Soc. Am*, **76**, 511-520.

Hearn, T M, X. Xiao, , J.F. Ni and the INDEPTH-III Team (2002). Crust and Mantle Structure Beneath the INDEPTH-III Central Tibet Array, *Eos AGU Trans. 2003 Fall Meet. Suppl.* **83(47)**, F1002.

Hearn, T.M., Wang, S., Ni, J.F., Xu, Z., Yu, Y. and X. Zhang (2004). Uppermost mantle velocities beneath China and surrounding regions *J. Geophys. Res.*, **109**, B11301, doi:10.1029/2003JB002874.

Kvaerna, T. and D.J. Doornbos (1991). Scattering of regional Pn by Moho topography, *Geophys. Res. Lett.*, **18**, 1273-1276.

Lay, T., X. Yang, X. Xie, S. Taylor and M. Arrowsmith (2006). Development of Regional Phase Tomographic Attenuation Models for Eurasia, in *Proc. 28th Seismic Research Review - Nuclear Explosion Monitoring: Ground-Based Nuclear Explosion Monitoring Technologies*, Orlando, Florida, 19-21 September 2006, National Nuclear Security Administration, LA-UR-06-5471, 71-81. 1-10

McNamara, D.T., T. Owens and W. Walter. (1995). Observations of regional phase propagation across the Tibetan Plateau, *J. Gephys. Res.* **100**, 22,215-22,229.

McNamara, D.T., W. Walter, T. Owens and C. Ammon (1997). Upper mantle structure beneath the Tibetan Plateau from Pn travel time tomography, *J. Gephys. Res.* **102**, 493-505.

Menke, W. and P.G. Richards (1980). Crust-mantle whispering gallery phases - a deterministic model of teleseismic Pn wave-propagation, *J. Gephys. Res.* **85**, 5416-5422.

Menke, W. and P.G. Richards (1983). The horizontal propagation of P-waves through scattering media - analog model studies relevant to long-range Pn propagation, *Bull. Seism. Soc. Am.*, **73**, 125-142.

Mitchell, B.J. (1995). Anelastic structure and evolution of the continental-crust and upper-mantle from seismic surface-wave attenuation *Rev. Geophys.*, **33**, 441-462.

Morozov, I.B. and S.B. Smithson (2000). Coda of long-range arrivals from nuclear explosions, *Bull. Seism. Soc. Am.*, **90**, 929-939.

Nelson, K.D., W. Zhao, L.D. Brown, J. Kuo, J. Che, X. Liu, S.L. Klemperer, Y. Makovsky, R. Meissner, J. Mechie, R. Kind, F. Wenzel, J. Ni, J. Nabelek, L. Chen, H. Tan, W. Wei, A.G. Jones, J. Booker, M. Unsworth, W.S.F. Kidd, M. Hauck, D. Alsdorf, A. Ross, M. Cogan, C. Wu, E. Sandvol and M. Edwards (1996). Partially Molten Middle Crust Beneath Southern Tibet: Synthesis of Project INDEPTH Results, *Science*, **274**, 1684-1687.

Ni, J. and M. Barazangi (1983). High-frequency seismic wave propagation beneath the Indian shield, Himalayan arc, Tibetan plateau and surrounding regions: high uppermost mantle velocities and efficient Sn propagation beneath Tibet, *Geophys. J. R. Astr. Soc*, **72**, 665-689.

Nielsen, L. and H. Thybo (2003). The origin of teleseismic Pn waves: Multiple crustal scattering of upper mantle whispering gallery phases, *J. Geophys. Res.*, **108(B10)**, 2460, doi:10.1029/2003JB002487.

Nowack, R.L. and S. Stacy (2002). Synthetic seismograms and wide-angle seismograms

attributes from the Gaussian beam and reflectivity methods for models with interfaces and gradients, *Pure and Applied Geophysics*, **159**, 1447-1464.

Owens T.J, G.E. Randall, F.T. Wu and R.S. Zeng (1993). PASSCAL Instrument performance during the Tibetan Plateau Passive Seismic experiment, *Bull. Seism. Soc. Am.*, **83**, 1959-1970.

Rapine R., F. Tilmann, M. West, J. Ni and A. Rodgers (2003). Crustal structure of northern and southern Tibet from surface wave dispersion analysis, *J. Geophys. Res.*, **108**, art. no. 2120.

Roecker, S.W., T.M. Sabitova, L.P. Vinnik, Y.A. Burmakov, M.I. Golyanov, R. Mamatkanova and L. Munirova (1993). Three-dimensional elastic wave structure of the western and central Tien Shan, *J. Geophys. Res.*, **98**, 15,779-15,795.

Ryberg, T., K. Fuchs, A.V. Egorkin and L. Solodilov (1995). Observation of high-frequency teleseismic Pn on the long-range Quartz Profile Across northern Eurasia, *J. Geophys. Res.*, **100**, 18151-18163.

Ruzaikin, A.I., I.L. Nersesov, V.I. Khalturin and P. Molnar (1977). Propagation of Lg and lateral variations of crustal structure in Asia, *J. Geophys. Res.*, **82**, 307-316.

Sereno, T.J., S.R. Bratt, and T.C. Bache (1988). Simultaneous inversion of regional wave spectra for attenuation and seismic moment in Scandinavia, *J. Geophys. Res.*, **93**, 2019-2036.

Sereno, T.J. and J.W. Given (1990). Pn attenuation for a spherically symmetric Earth model, *Geophys. Res. Lett.*, **17**, 1141-1144.

Tilmann, F., J. Ni and the INDEPTH III Seismic Team, (2003). Seismic imaging of the downwelling Indian lithosphere beneath central Tibet, *Science*, **300(5624)**, 1424-1427.

Tinker, M.A. and T.C. Wallace (1997). Regional phase development of the non-proliferation experiment within the western United States, *Bull. Seism. Soc. Am.*, **87**, 383-395.

Xie, J. (1996). Synthetic and observational study of Pn excitation and propagation in central Asia, *Phillips Laboratory Scientific Report No. 1*, PL-TR-96-2270, 24 pp., http://www.ldeo.columbia.edu/~xie/xie96.pdf (last accessed January, 2007).

Xie, J. (2003). Pn Q under Tibet and Tienshan with practical and scientific implications, in *Proc. 25th Seismic Research Review - Nuclear Explosion Monitoring: Building the Knowledge Base*, Tuscon, Arizona, 23-25 September 2003, National Nuclear Security Administration, LA-UR-03-6029.182-190.

Xie, J. and H. Patton (1999). Regional Phase Excitation and Propagation in the Lop Nor Region of Central Asia and Implications for the Physical Basis of P/Lg Discriminants, *J. Geophys. Res.*, **104**, 941-954.

Xie, J., R. Gok, J. Ni, and Y. Aoki (2004). Lateral variations of crustal seismic attenuation along the INDEPTH Profiles in Tibet from Lg Q inversion, *J. Geophys. Res.*, **109**, B10308, doi:10.1029/2004JB002988.

Yang, X, T. Lay and X-B Xie (2007) Geometric Spreading of Pn and Sn in a Spherical Earth Model, *Bull. Seismol. Soc. Am.*, submitted.

Zhao, X. and J.E. Ebel (1991). Radiation pattern of crustal phases of New England earthquakes, *Geophys. J. Int.*, **106**, 647-655.

Zhao, L.S. and J. Xie, (1993). Lateral variations in compressional velocities beneath the

Tibetan Plateau from Pn travel time tomography, *Geophys. J. Int.*, **115**, 1070-1084.

Zhu, T.F., K.Y. Chun and G.F. West (1991). Geometrical spreading and Q of Pn waves: An investigative study in eastern Canada. *Bull. Seismol. Soc. Am.*, **81**, 882-896.

AFFILIATION

Air Force Research Laboratory
Hanscom Air Force Base, Massachusetts, USA
jiakang.xie@hanscom.af.mil

Appendix
Potential Radiation Pattern from the 1999 Earthquake

In theory, Pn spectra from earthquake 99.030 may be affected by a non-isotropic source radiation pattern ($R(\theta)$ in equation (2)). In this appendix we demonstrate that the effect of this pattern is small and, when ignored, should not have caused significant errors in Pn Q estimates. First we note that this study uses finite Pn wavetrains, which are less vulnerable to the radiation pattern than are the first Pn pulses (Zhao and Ebel, 1993). To further explore the level of the radiation pattern from event 99.030, we calculate synthetic Pn wavetrains using (1) 1-D velocity model "M1" by Roecker et al. (1993), and (2) the centroid moment-tensor (CMT) solutions by Harvard and U.S. Geological Survey; both solutions characterizing the source as an obliquely reverse rupture. These synthetics are then used to predict Pn radiation pattern to the directions of KNET and INDEPTH III stations (roughly west and south, respectively). The radiation predicted using the Harvard solution is about 30% higher to KNET than to INDEPTH III stations. An almost exactly opposite prediction is obtained using the USGS solution. Perturbing the 1D velocity model and focal solutions cause variations of the predictions, but the range of the variations is small, presumably because neither station group is near the Pn nodal planes. Variations in radiation pattern of such level (±30% when comparing the KNET paths to the INDEPTH paths) are less than the observed spectral variations within each station group (Figure 4). We can estimate the relative error in Pn Q_0 measurement caused by an error δx arising from an unaccounted $R(\theta)$ of 1.3, using equation (A8) of Xie et al. (2004). Assuming δx=0.3, V=7.6 km/s, f=1 Hz, and Δ=1200 km, we obtain $\delta Q_0/Q_0$ of 16% and 11% when the true Q_0 is 260 and 175, respectively. These relative errors in Q_0 are rather small and acceptable. In the true Earth structure, 3D scattering should occur to further smooth-out any radiation pattern at the high-frequencies.

Next we empirically examine whether by ignoring the effect of non-isotropic $R(\theta)$, our estimates of Q_0 and η to the INDEPTH III stations are significantly biased (see section "Estimates of Apparent Pn Q to Indepth Stations"). Because group III-1 of stations are located in southern Tibet and are close to the INDEPTH II stations (here after referred to as "group II"; see Figures 1 and 5), the Pn Q_0 and η from the October 7, 1994 explosion (which should not have a non-isotropic $R(\theta)$) to station group II should be similar to those from earthquake 99.030 to station group III-1. If there is a significantly non-

isotropic $R(\theta)$ by event 99.030, then ignoring it should result in a biased set of Q_0 and η estimates over paths to group III-1. The bias should have masked the similarity between Q_0 and η values to group III-1 and those to group II. In the main text we ignored $R(\theta)$ and estimated average Q_0 and η values to station group III-1 to be 255±48 and 0.1±0.1, respectively. These values are close to those of 253±53 and 0.0±0.1, estimated for paths to station group II. This preserved similarity empirically demonstrates that a potential bias in the the estimated Q_0 and η values, caused by a non-isotropic $R(\theta)$ from event 99.030, is small. As a further precaution, we repeated the procedure of estimating Q_0 and η values using the southern half (8) stations of the 15-station group III-1. These 8 stations are even closer to the INDEPTH II stations as they tend to overlap (Figures 1 and 5). We obtained average Q_0 and η estimates of 258±42 and 0.0±0.1, respectively. These values are similar to those obtained using all 15 III-1 stations and show that our empirical inference on small $R(\theta)$ is robust.

Figure Captions

Figure 1. Map of study area. See inset annotation for symbols representing tectonic boundaries and seismic stations. The Sino-U.S. (91-92) and INDEPTH II and III stations were temporarily deployed during three PASSCAL experiments in Tibet. The Khyrghistan Network (KNET) is a permanent network. Regional earthquakes used in this study are shown as open circles. Earthquakes whose ID numbers start with 91 and 92 occurred in years 1991 and 1992 (see Table 2 of McNamara et al., 1995 for the event parameters). Earthquake 99.030 is an M_W=5.5 (m_b=5.9) event that occurred on January 30, 1999, at 3:51:5.4 UT. Stars are the June 10 and October 7, 1994 Lop Nor explosions (Table 1 of Xie and Patton, 1999). White, medium and dark grays represent elevations of greater than 4000 M, between 2000-4000 M, and less than 2000 M, respectively. The abbreviations are: MTB - Main Thrust Belt, IYS - Indus Yalong Suture; BNS - Banggong-Nujiang Suture; JRS - Jinsha River Suture, KF - Kunlun Fault, ATF - Altyn Tagh Fault, LTS - Lop Nor Test Site.

Figure 2. Vertical component record section from the INDEPTH II stations recording the October 7, 1994 explosion (m_b=5.9). Predicted arrival times corresponding to approximate Pn and Lg group velocities of 7.6 and 3.5 km/s are marked by gray lines. Lg is blocked. See Figure 3 of Xie and Patton (1999) for the record section from the KNET.

Figure 3. Time series containing the Pn wavetrain and the preceding noise (top), and Fourier spectra (bottom) from INDEPTH II station BB15 recording the October 7 explosion. For clarity, only two of the five signal windows (the first and third windows) are shown by the dashed curves on the top. Upper and lower black curves in the bottom are spectra from individual signal and noise windows. The spectrum in gray is the average of the Pn signal spectra.

Figure 4. Pn spectra from explosions and earthquake in the Lop Nor region of eastern Tarim Basin. Spectra are scaled by $\Delta^{1.3}$ to reduce the effect of geometrical spreading. Each row is from one event as indicated at lower left, with "EX" and "EQ" indicating explosions and earthquake (see Figure 1). The INDEPTH III stations are divided into two groups (III-1 in row 3 and III-2 in row 4), located to the south and north of the BNS (Figures 1 and 5). Left columns show individual spectra from KNET and INDEPTH networks as black and gray curves, with the network name and number of recording stations written nearby. Right columns show the network averaged spectra and the associated sample standard deviations. The average distances are marked.

Figure 5. Map showing paths used in this study and the estimated Pn Q_0 and η values. The events and stations are the same as those plotted in Figure 1. Black paths are from earthquake 99.030 to station group III-2, sampling the northern Tibetan Plateau. Light gray paths are those from the 1994 explosions to INDEPTH II stations, or from earthquake 99.030 to station group III-1, sampling a mixture of northern and southern Tibetan Plateau. White paths are from explosions and earthquake 99.030 to KNET. Dashed lines plotted in darker gray are paths from the regional earthquakes to the 1991-1992 PASS-CAL stations, used in the two-station Pn Q measurements. Three profiles are formed: SANG-TUNL, WNDO-TUNL which is a subprofile of SANG-TUNL, and
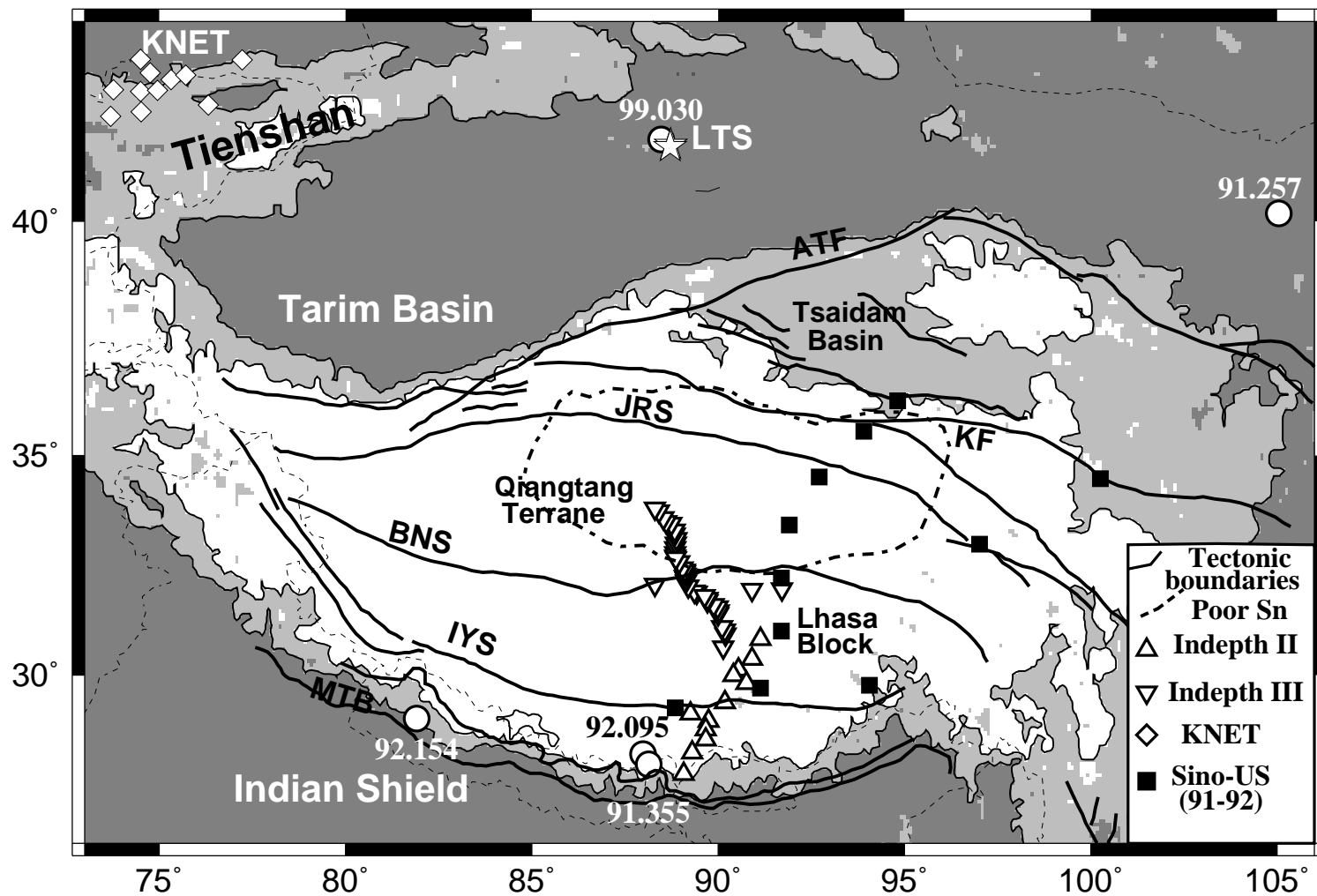
SANG/GANZ-MAQI which is merged from two sub-profiles SANG-MAQI and GANZ-MAQI. The end stations along these profiles (SANG, TUNL, WNDO, SANG, GANZ and MAQI) are written. See McNamara et al. (1995) for other station names. The Pn Q_0 and η values are written near the paths over which they are estimated (values for paths in gray are the average to station groups II and III-1); oblique numbers are those obtained using the two-station method.

Figure 6. Network averaged Pn spectra (fluctuating curves), and the model spectra (smooth curves) corresponding to rows 1, 3 and 4 of Figure 4. Model spectra are constructed using the MMM or Brune source model, the estimated source M_0, f_c and path-averaged Q_0 and η values. Similarly to Figure 4, black and gray are used for spectra from KNET and INDEPTH networks. The network name and path-averaged Q_0 and η values are written near the curves. Note that only 8 KNET stations recorded the October 7 explosion, so the average Q_0 is 381, rather than 364 obtained using all 10 KNET stations (Xie and Patton, 1999).

Figure 7. Stacked spectral ratios (SSRs) calculated along three profiles in eastern Tibet (dots) and the best-fitting models of Q_0 and η (straight lines). Profile names and numbers of two-station pairs used are written on the top of each panel (see Figure 5 for profile locations). The frequency bands used, and estimated Q_0 and η values are written inside the panels.
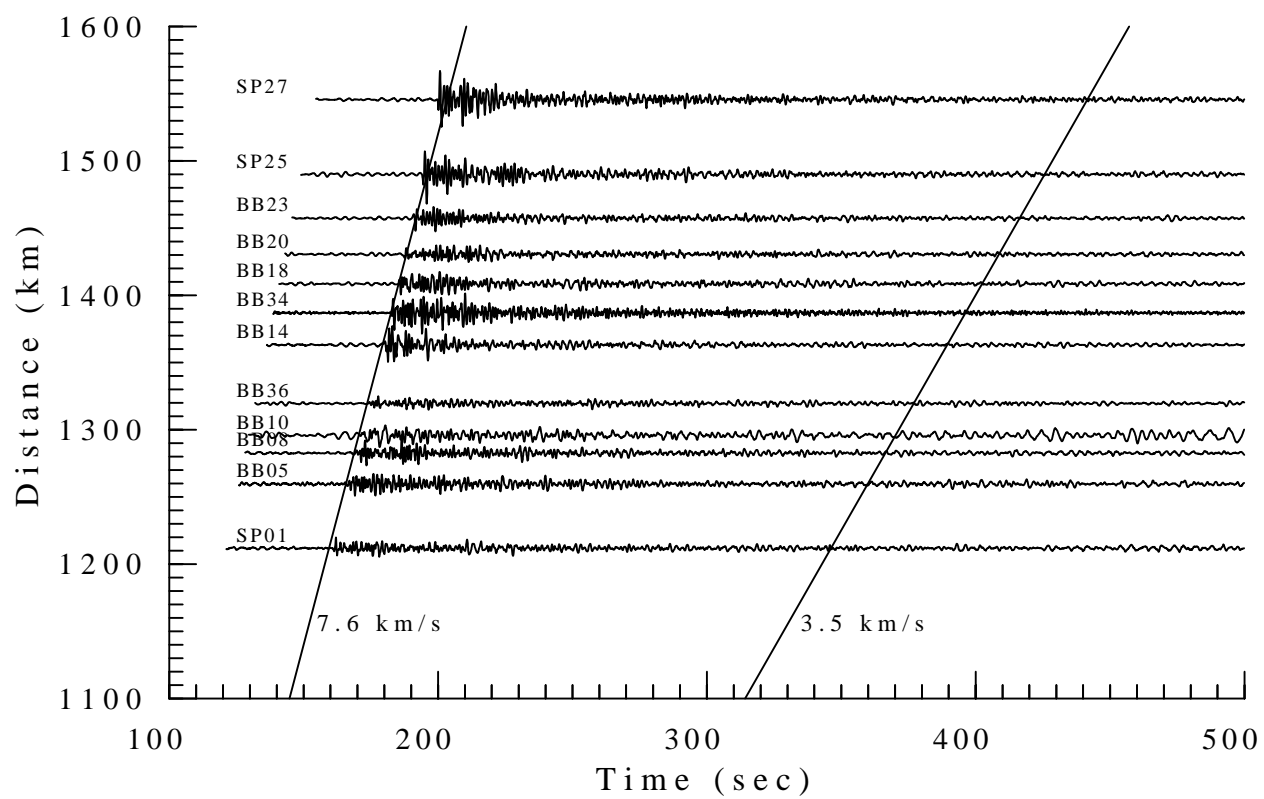
Figure 8. Pn attenuation models calculated for various regions from published observations, at a reference distance of 1200 km. Each model is plotted in the frequency range of observation. Model "Canadian S." is for the Canadian shield, calculated using the Q_0 and η values and the G.S.T. by Zhu et al. (1991). Model "Scandinavia" is from Sereno et al. (1988). Model "C. Asia" is for central Asia (Xie and Patton, 1999; this study). Models "C. TP." and "N. TP." are obtained from this study for paths running from LTS to stations in south-central Tibet and north-central Tibet (gray and black paths in Figure 5), respectively. Values of Q_0 and η of the models obtained in this study are written. Models for east Tibet (along profile SANG-TUNL in Figure 5) and easternmost Tibet (along profile SANG/GANZ-MAQI), both obtained in this study are not plotted because they are similar to Models C. TP and C. Asia (see section "Apparent Pn Q along Passcal Profiles in Eastern Tibet"), respectively.

Figure 9. Stacked spectral ratios (SSRs) calculated along profile SANG-TUNL using a G.S.T. correction of $m=1.07+0.035f$ (in gray), versus SSRs with a G.S.T. correction of $m=1.3$ (in black; the same as in the top panel of Figure 7). The best fit Q_0 and η models and resulting residuals are indicated. The residuals differ from each other by less than 0.2%, indicating a virtually complete trade-off between G.S.T. and Q_0 and η for the data used in this study. The former G.S.T. is estimated for the Canadian shield by Zhu et al (1991) and is used here to illustrate the parameter trade-off.
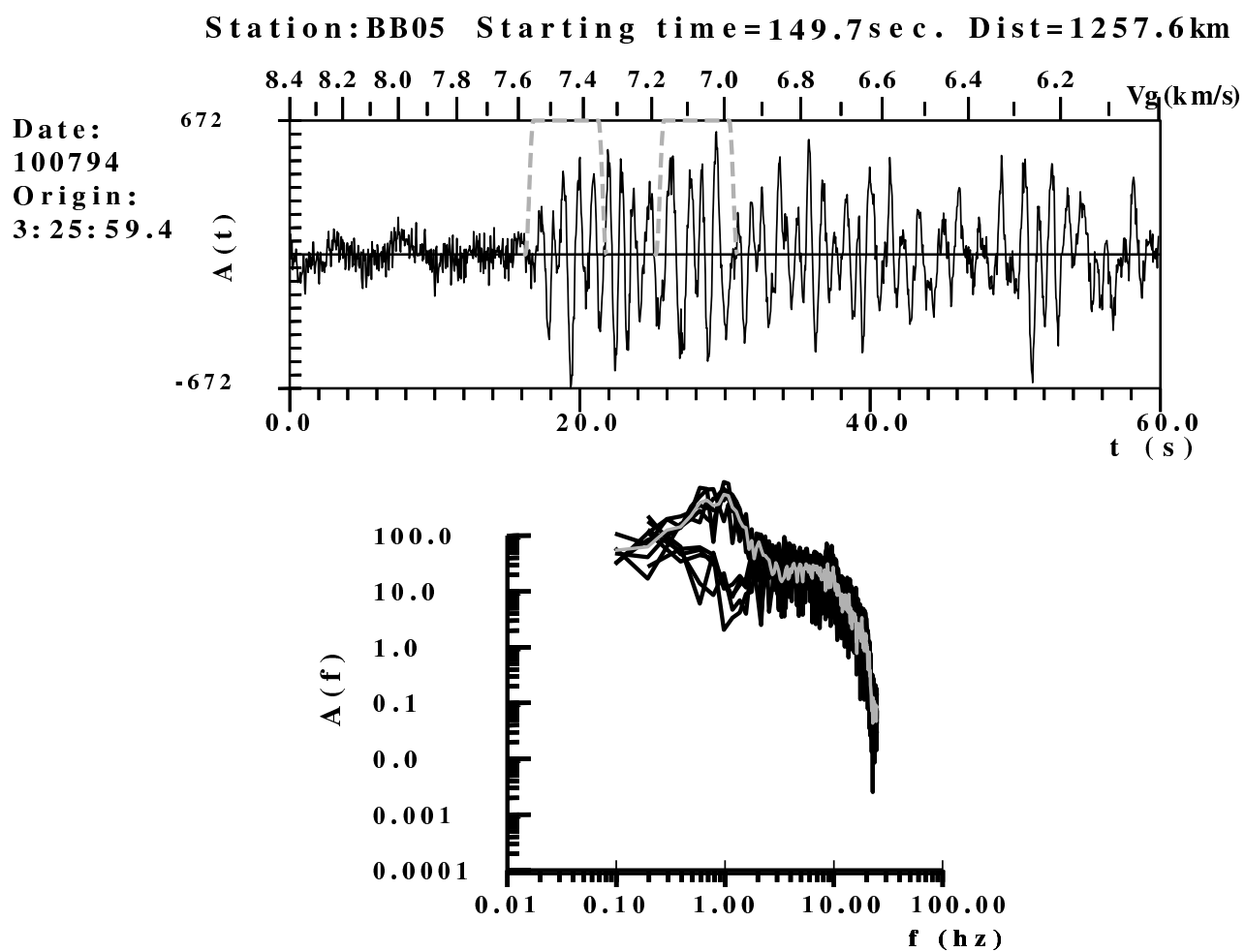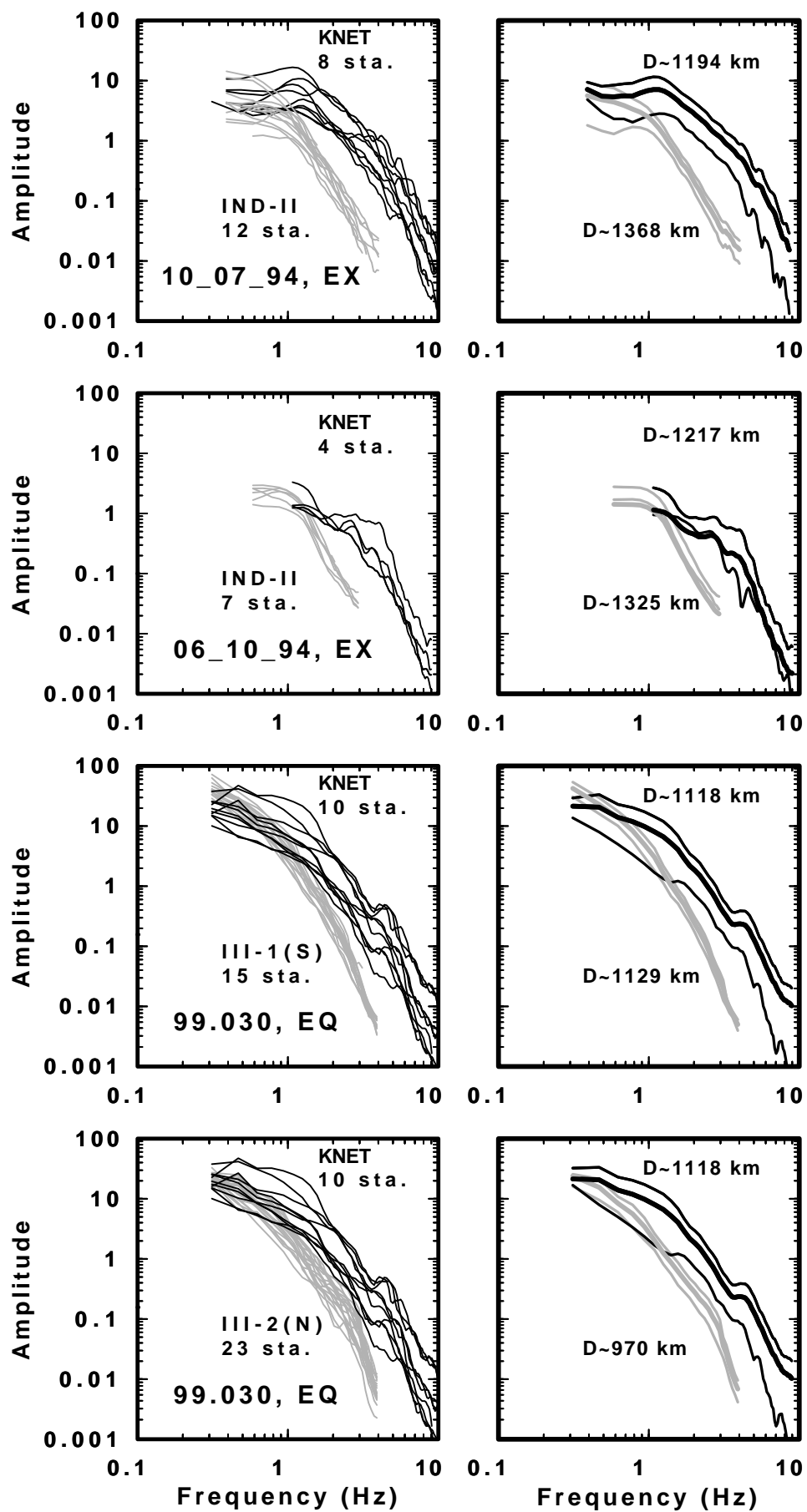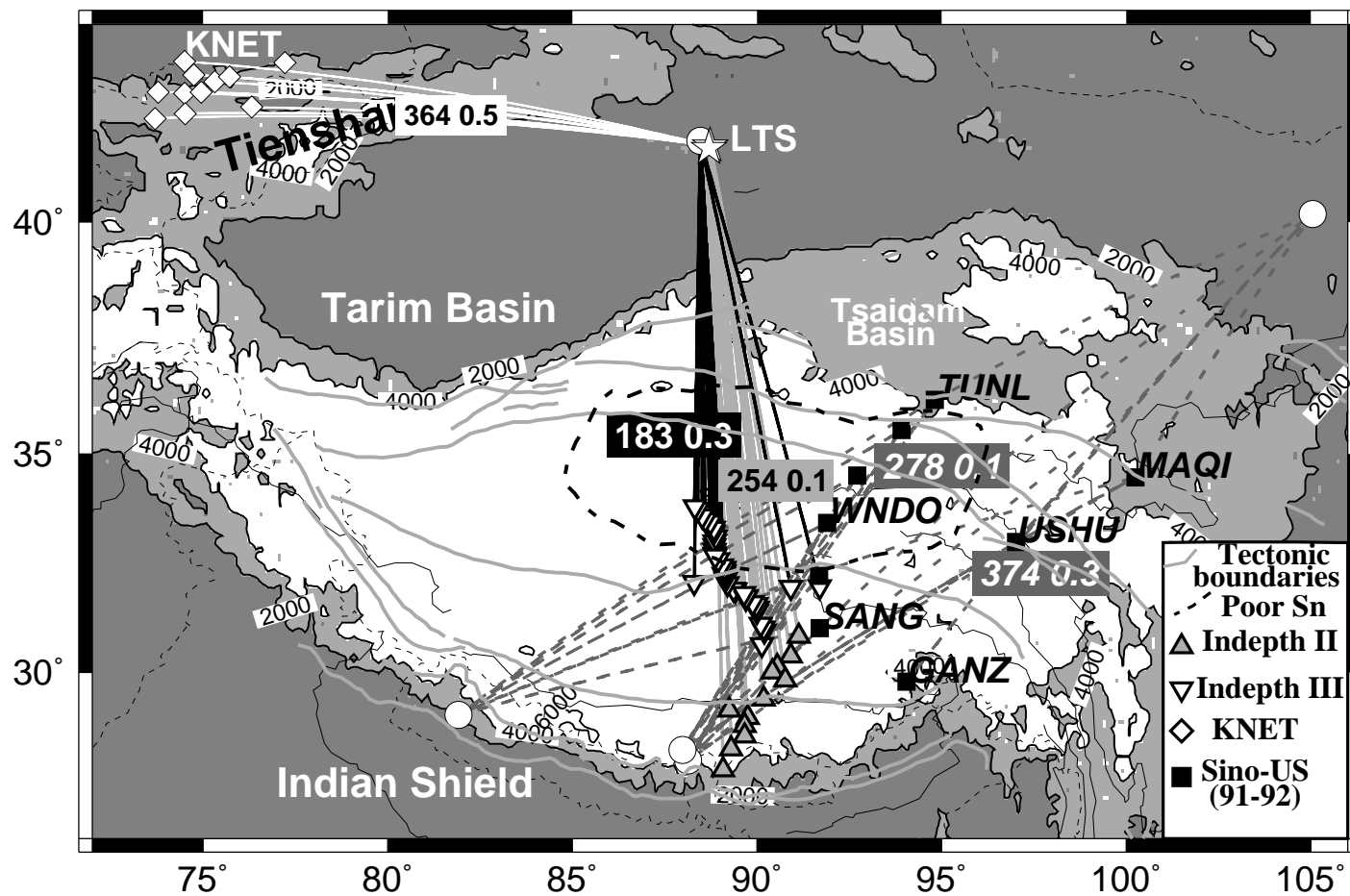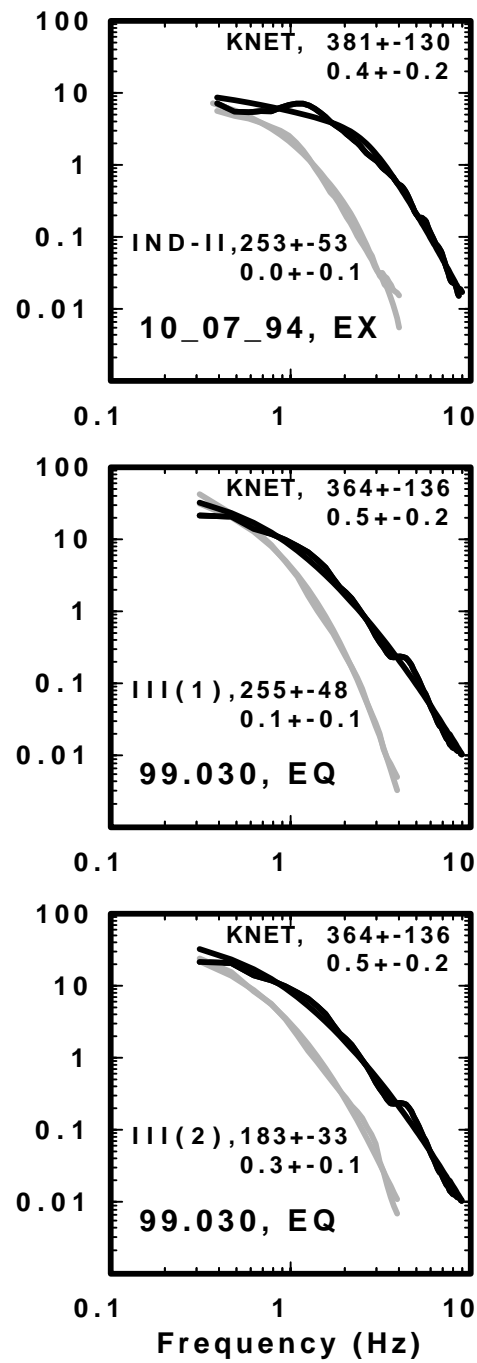
Xie 2006, Fig. 1.

Xie 2006, Fig. 2.

Station:BB05 Starting time=149.7sec. Dist=1257.6km

Date:
100794
Origin:
3:25:59.4

Xie 2006, Fig. 3.

Xie 2006, Fig. 4.

KNET

Tienshan

364 0.5

LTS

40°

Tarim Basin

Tsaidam Basin

4000

2000

TUNL

183 0.3

254 0.1

278 0.1

MAQI

35°

WNDO

USHU

374 0.3

SANG

Tectonic boundaries

Poor Sn

△ Indepth II

▽ Indepth III

◇ KNET

■ Sino-US (91-92)

30°

GANZ

Indian Shield

2000

75°   80°   85°   90°   95°   100°   105°

Xie 2006, Fig. 5.

Xie 2006, Fig. 6.

SANG-TUNL,39 pairs

0.7-4.5 Hz
Qo=278+-23
eta=0.1+-0.1

WNDO-TUNL,18 pairs

0.7-4.5 Hz
Qo=273+-32
eta=0.0+-0.1

SANG/GANZ-MAQI,11 pairs

0.5-6.0 Hz
Qo=374+-57
eta=0.3+-0.1

Xie 2006, Fig. 7.

Xie 2006, Fig. 8.

SANG-TUNL, 0.7-4.5hz

m=1.07+0.035f:
Q0=241,eta=.20
Res.=0.6647

m=1.3:
Q0=278, eta=.14
Res.=0.6660

f**(1-eta)/Qo

Frequency(hz)
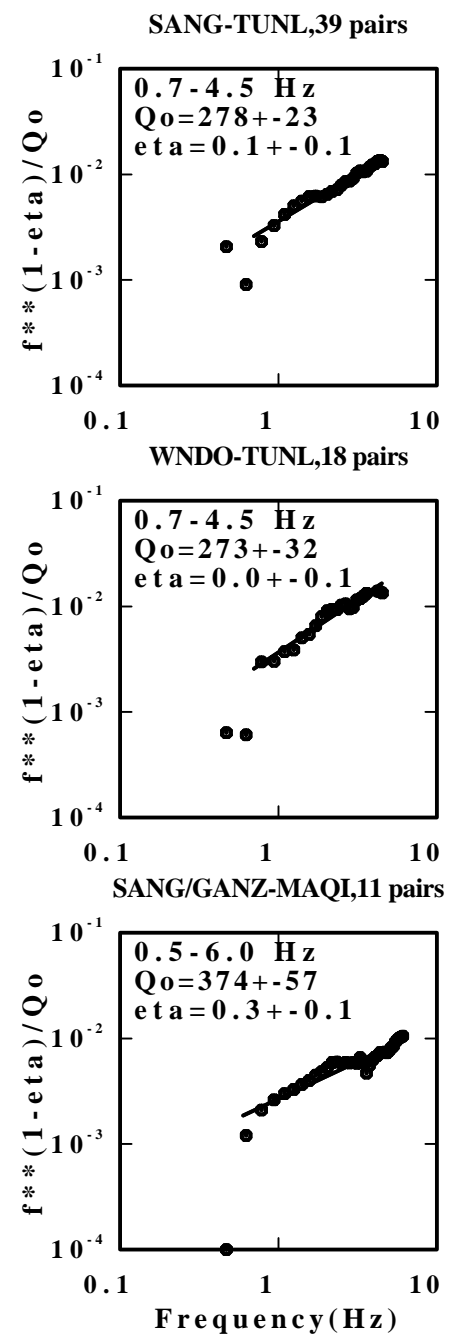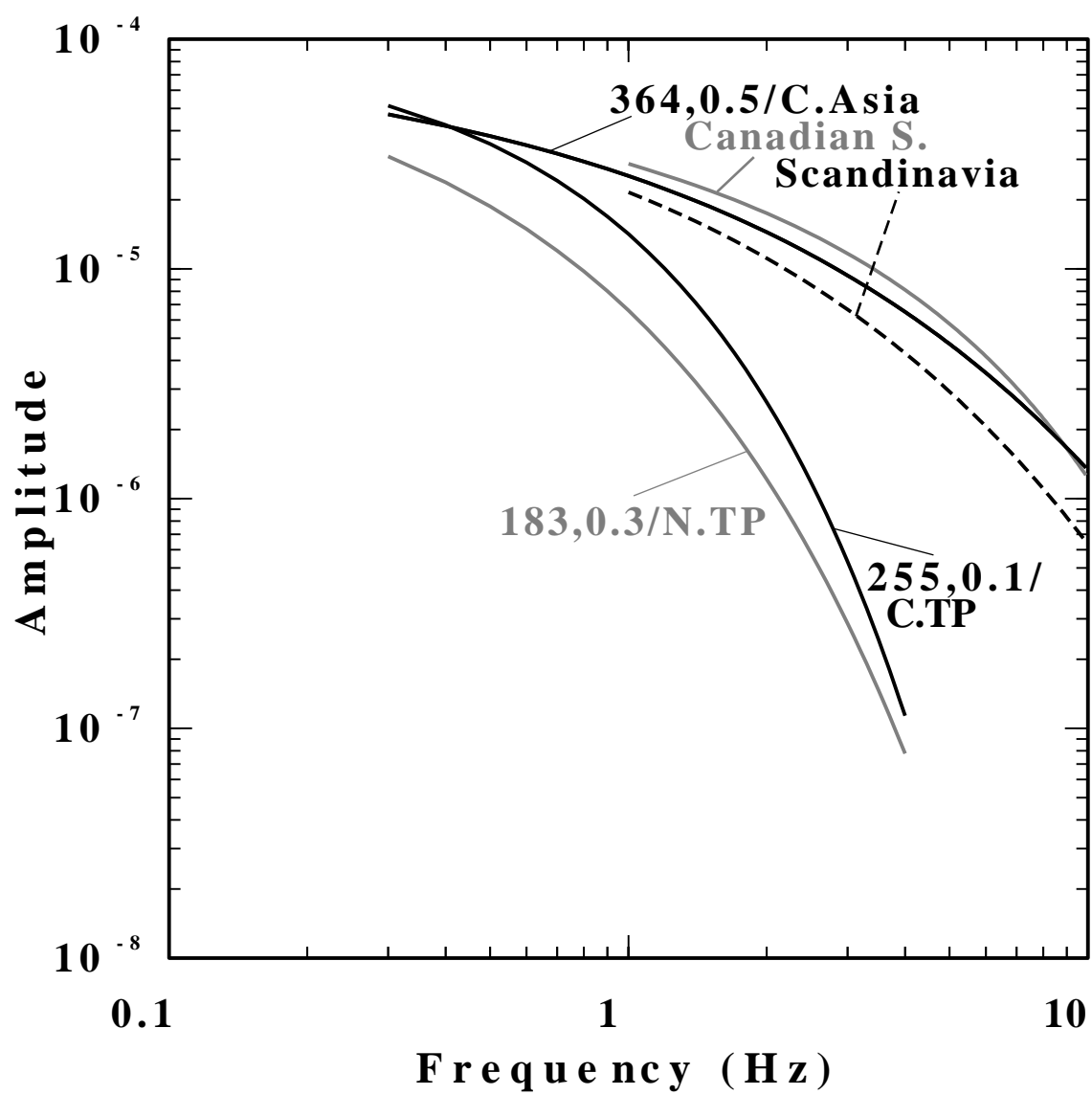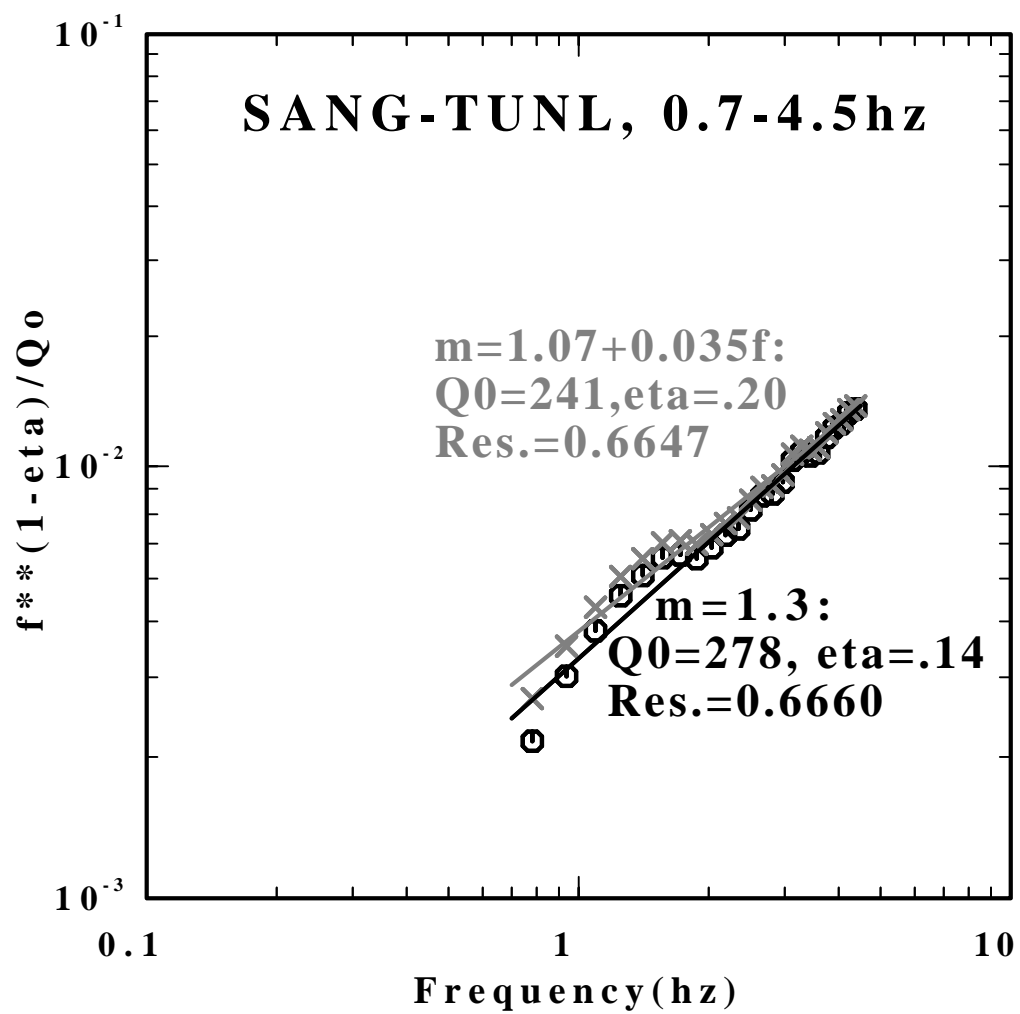
Xie 2006, Fig. 9.

Appendix C.
Crust and Upper Mantle Shear-Velocity and Q_μ Structure in Eastern Eurasia from
Rayleigh-wave Phase and Amplitude Data
J. Gaherty, P. Chen, L. Zhao, and T.-K. Hong

Crust and Upper Mantle Shear-Velocity and Q_μ Structure in Eastern Eurasia from Rayleigh-wave Phase and Amplitude Data

James B. Gaherty[1], Po Chen[1], Li Zhao[2], and Tae-Kyung Hong[1,3]
[1]Lamont-Doherty Earth Observatory of Columbia University
[2]Institute of Earth Sciences, Academia Sinica, Taiwan
[3]Yonsei University, Korea

Abstract

We have mapped lateral variations of crustal and upper-mantle shear-wave velocity β and shear attenuation ($1/Q_\mu$) in eastern Eurasia using a new joint inversion procedure based on three-dimensional partial-derivative (Fréchet) kernels. In our analysis, we utilized Rayleigh waves with periods longer than ~15 s, derived from regional and near-teleseismic earthquakes. We collected and analyzed 859 vertical-component seismograms, derived from over 133 events with $M_w \geq 5.5$ that occurred within the eastern Eurasia region (10˚-60˚N, 70˚-140˚E) between 2000-2006. The data were recorded on 71 broadband seismic stations within eastern Eurasia (10˚-60˚N, 80˚-140˚E). The seismograms were evaluated for signal-to-noise within the band of interest (10 mHz – 80 mHz) by comparing the records to complete normal-mode synthetic seismograms for radially symmetric and transversely anisotropic reference models. We then made 15,462 mutually consistent measurements of frequency-dependent traveltime and amplitude anomalies for surface waves by cross-correlation between records and synthetics. We used coupled normal-mode summation to compute the three-dimensional Fréchet kernels of these traveltime and amplitude anomalies to both the elastic shear-wave speeds β and shear-wave quality factor Q_μ values. Our starting model for Q_μ was extracted from a recent global model of upper-mantle attenuation. The frequency-dependent traveltime and amplitude anomalies were jointly inverted for three-dimensional models of both elastic and anelastic structures. This coupled inversion allowed us to account for the effects on amplitudes from elastic heterogeneities such as scattering, focusing and defocusing, as well as the effects of anelastic dispersion on the traveltimes. The regional models we have obtained provide lateral resolution of about 400 km in the crust and upper mantle. In the crust, high values of Q_μ are concentrated in eastern China, extending southward from the north China craton, while a clear low-Q anomaly in the crust beneath northern Tibet. In the upper mantle, the model is characterized by a lithosphere with very high Q values ranging from 250-400, underlain by a low-Q asthenosphere with Q_μ of 60-100. The lateral variation of the upper-mantle Q_μ perturbation appears to correlate with the lateral variation in the inverted shear-velocity perturbation.

Introduction

Accurate event detection, identification, and characterization are critical components of the US nuclear monitoring program. A necessity for improving these estimates is the more accurate estimation of seismic attenuation rate (or its inverse, Q), which controls the amplitudes of seismic phases upon which the assessments are based.

Q is known to vary widely in continental regions, making reliable estimates of it critically important, but also quite difficult. Q is also frequency dependent, which makes it difficult to determine whether Q estimates derived from different phases with different frequency characteristics are a result of intrinsic frequency dependence, or differences in structural sampling. Finally, Q estimates are derived from seismic amplitudes, which are also strongly dependent on elastic effects such as wavefield focusing and scattering. As a result, robust tomographic (3D) quantification of Q on regional scales remains in its infancy.

We address this problem by developing and applying a comprehensive waveform analysis and inversion scheme to simultaneously estimate 3D variations in shear velocity (β) and shear-wave attenuation (or more precisely, its inverse, the shear-wave quality factor Q_μ) from Rayleigh waves recorded in eastern Eurasia. The analysis technique characterizes phase and amplitude residuals between recorded and synthetic Rayleigh waves, and inverts them using new three-dimensional sensitivity (Fréchet) kernels for structural perturbations. The analysis spans a frequency band from 0.01-0.05 Hz, with the low frequency estimates providing a stable long-wavelength framework from which we bootstrap to higher frequency. We focus on Rayleigh waves because they provide self-consistent spatial and depth constraints on Q_μ in the crust and upper mantle across a broad frequency band. In Eurasia, Rayleigh waves from regional and near-teleseismic events give good spatial coverage, and can quantify large-scale regional trends and the effects of long-wavelength scattering. The resulting model spans all of China, the Korean peninsula, and much of Southeast Asia, and can be used to place localized high-frequency observations (e.g. L_g, P_g, S_n, P_n) into a larger regional context.

Data Collection

Our data set consists of broadband Rayleigh waves that traverse Eastern Eurasia. The seismic records were recorded on instruments from the IRIS GSN, cooperating networks such as the CDSN, and several IRIS PASSCAL experiments from Asia. All data were collected from IRIS DMC. The stations used are distributed in the region from 10˚N - 60˚N and 80˚E - 140˚E. We used stations recording either an LHZ or BHZ component, with a total of 71 stations. Events occurred in the region between 10˚N - 60˚N and 70˚E - 140˚E in the time period between 2000 and 2006. The magnitudes are greater than M_w 5.5. The initial dataset was cleaned to remove data with a signal-to-noise level of less than approximately 2 in the central portion of the frequency band (0.02-0.1 Hz), as well as data clearly contaminated by glitches or other problems. The final number of records used is 859 from 133 events. The final event and station distribution as well as the spatial path coverage associated with this data is shown in Figure 1.

Methodology

We analyzed the selected seismograms using the *generalized seismological data functionals* (GSDF) method (Gee and Jordan, 1992; Gaherty et al., 1996), where the phase-delay times $\delta t_p(\omega_n)$ and differential amplitudes $\delta t_q(\omega_n)$ of observed Rayleigh waves were measured relative to complete normal-mode synthetic seismograms as a function of frequency ω_n across the 0.01-0.05 Hz band. This methodology utilizes synthetic

seismograms of a target wavegroup (in this case the fundamental-mode Rayleigh waves) to estimate phase delays and relative amplitudes of the observed arrival relative to the synthetic as a function of frequency. An example of the GSDF processing is shown in Figure 2. To make the GSDF measurements, the synthetic wavegroup, called an "isolation filter", is cross-correlated with both the data and a complete synthetic seismogram. The resulting cross-correlagrams are windowed and narrow-band (Gaussian) filtered at discrete frequency intervals between 0.01 and 0.05 Hz, and the peak phase and amplitude of each correlagram is estimated at each frequency. Referencing the observations to a synthetic/isolation-filter cross-correlation in this fashion allows us to account for interference from unmodeled wavegroups and minimizes bias associated with windowing and filtering. The synthetics are complete from 0-50 mHz (all periods longer than 12.5 s), and are calculated for a reference models (Figure 3) constructed from a composite of IASP91 for mantle shear and compressional velocities; Crust 2.0 for local crustal velocity perturbations (Laske et al., 2001); a mantle Q_μ profile for the China region extracted from a recent global model (Dalton and Ekström, 2006); and a crustal Q_μ profile derived from analysis of regional phases (Jemberie and Mitchell, 2004).

These observations characterize the observed wavefield characteristics in a manner similar to traditional estimates of phase velocity and spectral amplitudes. They differ from the traditional estimates in that they are relative to a reference model (similar to travel-time residuals), and thus can be directly inverted for improved velocity and Q structure using a linearized Gaussian-Bayesian approach (e.g. Gaherty et al., 1996). In the frequency domain, we can map the synthetic waveform $u_i(\omega)$ into the observed waveform $\bar{u}_i(\omega)$ using two frequency-dependent, time-like quantities $\delta\tau_p(\omega)$ and $\delta\tau_q(\omega)$

$$\bar{u}_i(\omega) = u_i(\omega)\exp\{i\omega[\delta\tau_p(\omega) + i\delta\tau_q(\omega)]\}. \tag{1}$$

The GSDF measurements of $\delta t_x(\omega_n)$ (x = p, q) are weighted averages of $\delta\tau_x$ over a narrow frequency-band centered on ω_n. As shown in Chen *et al.* (2006), these frequency-dependent GSDF measurements can completely capture the waveform information if the sampling in frequency domain is dense enough. And the GSDF measurements are well suited for the tomographic inverse problem. In particular, their linearization is based on the Rytov approximation, which is valid for large accumulative phase-shifts as long as the phase perturbation *per wavelength* is small (Chernov 1960; Snieder & Lomax 1996). This is much less restrictive than the Born approximation, which requires small accumulative phase-shifts.

The sensitivity (Fréchet) kernels for our GSDF measurements with respect to shear-wave velocity β and attenuation Q_μ were computed using the "full wave" approach of Zhao & Jordan (2006). First, we linearize the relation between GSDF measurements and waveform perturbation

$$\delta d_{in}^{sr} = \int dt \, J_{in}^{sr}(t) \, \delta u_i^s(\mathbf{x}_r, t), \tag{2}$$

where d_{in}^{sr} as the n-th GSDF measurement made on the i-th component of the seismogram, which is generated by source s and recorded at receiver r. Exact expressions of the seismogram functional $J_{in}^{sr}(t)$ for GSDF measurements are give in Chen (2005). Second, we linearize the relation between waveform perturbation and the perturbation to the density $\delta\rho(\boldsymbol{x})$ and elastic/anelastic modulus tensor $\delta c_{jklm}(\boldsymbol{x})$ using the Born approximation

$$
\delta u_i^s(\boldsymbol{x}_r, t) = -\int dV(\boldsymbol{x}) \int d\tau \left\{ \sum_j [G_{ij}(\boldsymbol{x}_r, t-\tau;\boldsymbol{x})\partial_\tau^2 u_j^s(\boldsymbol{x},\tau)\delta\rho(\boldsymbol{x}) \right.
$$
$$
\left. + \sum_{jklm} \partial_k G_{ij}(\boldsymbol{x}_r, t-\tau;\boldsymbol{x})\,\partial_l u_m^s(\boldsymbol{x},\tau)\delta c_{jklm}(\boldsymbol{x})] \right\}
$$
(3)

The exact Fréchet kernels for GSDF measurements can therefore be expressed as

$$
K_{d_{in}^{sr}}^{\rho}(\mathbf{x}) = -\int dt \int d\tau J_{in}^{sr}(t) \sum_j G_{ji}(\mathbf{x}, t-\tau;\mathbf{x}_r)\partial_\tau^2 u_j^s(\mathbf{x},\tau),
$$
(4)

$$
K_{d_{in}^{sr}}^{c_{jklm}}(\mathbf{x}) = -\int dt \int d\tau J_{in}^{sr}(t)\partial_k G_{ji}(\mathbf{x}, t-\tau;\mathbf{x}_r)\partial_l u_m^s(\mathbf{x},\tau),
$$
(5)

which generally involves the convolution between gradients of the forward earthquake wavefields $u_m^s(\mathbf{x},t)$ with the gradient of the transposed "receiver Green tensor" (RGT) $G_{ji}(\mathbf{x},t;\mathbf{x}_r)$ (Zhao $et\ al.$ 2006). Because both the forward earthquake wavefields and the RGTs were computed using the normal-mode theory, which provides the exact solution to the wave equation in a 1D reference model, the Fréchet kernels constructed this way can account for the full physics of wave propagation including multipathing and non-geometrical arrivals (Zhao & Jordan 2006).

When intrinsic attenuation is taken into account, the (real) elasticity tensor is replaced by a complex tensor:

$$
C_{jklm} = \left\{ \kappa(\omega)[1+iQ_\kappa^{-1}(\omega)] - \frac{2}{3}\mu(\omega)[1+iQ_\mu^{-1}(\omega)] \right\} \delta_{jk}\delta_{lm}
$$
$$
+ \mu(\omega)[1+iQ_\mu^{-1}(\omega)](\delta_{jl}\delta_{km}+\delta_{jm}\delta_{kl}) + \gamma_{jklm},
$$
(6)

where Q_κ and Q_μ are the quality factors for the incompressibility κ and the shear modulus μ, respectively. In (6), the elasticity tensor has been decomposed into a purely isotropic part expressed in terms of κ and μ and a purely anisotropic part γ_{jklm}, and the intrinsic attenuation of only the purely isotropic part is considered (Dahlen & Tromp 1998). Substituting the complex tensor in equation (6) into equation (3), we can obtain a linearized relation between the waveform perturbation $\delta u_i^s(\boldsymbol{x}_r, t)$ and the perturbations δQ_κ and δQ_μ. From this linearized relation and equation (2) we can derive the expressions for the Fréchet kernels of the GSDF measurements with respect to the shear-wave

velocity β and attenuation factor Q_{μ}. Figure 4 shows examples of Fréchet kernels of phase-delay time δt_p with respect to shear-wave velocity and amplitude-reduction time δt_q with respect to shear-wave velocity and Q_{μ} for a Rayleigh wave at 35 mHz.

Results

We made 7,731 frequency-dependent phase-delay time (δt_p) and 7,731 amplitude anomaly measurements (δt_q) for the Rayleigh waves on the selected 859 high-quality vertical-component seismograms at 9 frequencies ranging from 10 mHz to 50 mHz. The 15,462 GSDF measurements were then inverted jointly for both shear-wave velocity perturbation $\delta\beta/\beta$ and attenuation perturbation $\delta Q_{\mu}/Q_{\mu}$ using the full-wave Fréchet kernels (Figure 4). This joint inversion for both shear velocity and attenuation allows us to account for the effects of scattering and focusing/defocusing effects on waveform amplitudes cause by elastic heterogeneities using the amplitude kernels with respect to shear velocity. The phase-delay measurements included in the inversion provide additional constraints on shear velocity. In this model, we do not incorporate the frequency-dependence of Qm; the derived models are appropriate for a center frequency of ~25 mHz, and assume constant Q over a frequency band of 0.01-0.06 Hz.

Our modeling volume extends from 70° E to 141° E in longitude, from 10° N to 58° N in latitude and from 0 km to 280 km in depth. We discretized the modeling volume into 2° by 2° blocks with a vertical dimension varying from 10 km at shallower depth to 40 km at larger depth. The model parameters are assumed to be constant within each block. This parameterization results in 21,600 model parameters considering both shear velocity perturbation $\delta\beta/\beta$ and attenuation perturbation $\delta Q_{\mu}/Q_{\mu}$. The sensitivity kernels, which were originally computed on a 1° by 1° grid with vertical grid spacing of 1 km, were then averaged over each 2° block. We introduced 266 additional model parameters to account for the unknown errors in source origin time and scalar moment for the 133 earthquakes used in this study. The total number of model parameters used in our inversion is 21,866.

The resulting linear system was then scaled using a data-weighting matrix $\mathbf{C}_d^{-1/2}$ and concatenated with the "roughing operator" $\mathbf{C}_m^{-1/2}$, which is a linear combination of the Laplacian operator (Constable *et al*. 1987; Sambridge 1990; Tarantola 2005) and the identity operator, i.e. $\mathbf{C}_m^{-1/2} = \theta(\mathbf{I} + \lambda\nabla^2)$. Using this definition of the "roughing operator", we impose our prior information on the inversion; i.e., we assume that in the absence of any other information, the model perturbation is smooth and small. We note that the corresponding "smoothing operator" $\mathbf{C}_m^{1/2}$ can be generated from an exponential correlation function, whose correlation length is proportional to λ. In practice, the Laplacian operator is approximated numerically by finite differencing. The final linear system that we solve is

$$\begin{vmatrix} \mathbf{C}_d^{-1/2}\mathbf{A} \\ \mathbf{C}_m^{-1/2} \end{vmatrix} \delta\mathbf{m} = \begin{vmatrix} \mathbf{C}_d^{-1/2}\mathbf{d} \\ 0 \end{vmatrix} \tag{7}$$

where matrix **A** contains the averaged sensitivity kernels for each GSDF measurement, $\delta\mathbf{m}$ is the model parameter vector and **d** is the data vector. The linear system specified by equation (7) was solved using a parallelized LSQR subroutine from the PETSc parallel scientific computing library (Balay *et al.* 2004). The LSQR method (Paige & Saunders 1982), which is a type of conjugate-gradient method, provides a very efficient means for solving large-scale sparse linear systems.

We have carried out a series of inversions to construct the trade-off curves between variance reduction and model smoothness (Figure 5). Our preferred model EAF3D locates around the corners of the trade-off curves. Figure 6 shows this preferred model at 12 different depths. This model provides a variance reduction of about 52% and is relatively smooth.

An important indicator of the resolution of our inversion is the spatial coverage of all the Fréchet kernels used in the inversion. In Figure 7, we have plotted the summation of the absolute values of all the kernels within each block of our modeling volume. The best kernel coverage is in the crust and upper mantle; the coverage is still decent down to a depth of about 170 km.

Discussion

In general, the inverted model perturbation EAF3D is geologically reasonable. For shear-velocity perturbation, the amplitude ranges from -5% to 5%. Spatially, the velocity model shows a broad region of low shear-wave speeds in central and western China that extend through the crust and upper mantle, with higher velocities to the east. These velocity anomalies are derived primarily to account for their effect on wave amplitude (and thus Q), and thus are not the focus of this study. For Q_μ perturbation, the amplitude ranges from -40% to 40%. In the crust, high values of Q_μ are concentrated in eastern China, extending southward from the north China craton. This result is in good agreement with variations observed by Jemborie and Mitchell (2004) from Rayleigh waves, and also generally agrees with the result of Xie et al., (2005) derived from high frequency Lg observations. A clear low-*Q* anomaly in the crust beneath northern Tibet is also in good agreement with previous studies (Jemborie and Mitchell, 2004; Xie et al., 2005), and the anomaly persists well into the upper mantle (Fig 6b).

A general feature of our inverted Q_μ perturbation is that at shallower depth in the lithosphere, the average perturbation is positive; while at larger depth in the asthenosphere, the average perturbation is negative. This inverted Q_μ perturbation seems to enhance the depth gradient that already exists in the 1D reference model (Figure 3). If we apply the inverted Q_μ perturbation to the 1D reference model, we obtain an updated 3D model that characterizes both the lateral and depth variation of the absolute value of Q_μ throughout the region (Figure 8). In the crust, Q_μ varies from a minimum of 75 to a maximum near 200. This is similar to the range observed by Jemborie and Mitchell (2004), although in detail their minimum value beneath Tibet is slightly slower (~40), and our maximum values beneath eastern China are slightly higher than theirs. These differences are likely due to resolution differences in the models. Jemborie and Mitchell likely contain better resolution in the upper crust, while our explicit inclusion of *Q*

variations in the mantle may result in improved Q_μ estimates in the lower crust. Further tests of these models are underway to evaluate this issue.

In the upper mantle, the model is characterized by very high Q values ranging from 250-400. This is largely driven by the high-Q region in eastern China. The result is robust, in that the starting model had a relatively high-Q lid (Figure 3), but the relative amplitude residuals for the Rayleigh-wave frequencies sensitive to lid structure clearly required even higher Q on average. As a result of model smoothness constraints, the absolute value of Q in the low Q region of western China is likely overestimated. Below the lid, the Q drops to very low values in the range of 60-100. Again, on average these values seem to be quite robust, as the amplitudes of the long-period Rayleigh waves were persistently low, despite the low-Q asthenosphere in the starting model. This sharp transition from a high-Q lid to a low-Q asthenosphere appears to persist throughout most of China at depths of 135 km and greater.

The lateral variation of the upper-mantle Q_μ perturbation seems to correlate with the lateral variation in the inverted shear-velocity perturbation. This result is consistent with the conclusion reached by Xie (2006) based on spectral analysis on P_n arrivals from 1 Hz to 10 Hz. In Xie (2006), this lateral variation of attenuation is interpreted as a result of temperature variation in the mantle lid under Tibet, i.e. the temperature in the mantle lid under northern Tibet is abnormally high and causes partial melting while it is abnormally low under southern and eastern Tibet due to the underthrusting Indian lithosphere.

We emphasize that these models are preliminary. We are currently updating the models by incorporating two improvements:

1. We are incorporating the effects of variable topography of major discontinuities such as the Moho. Explicit expressions for the Fréchet kernels of the waveform with respect to discontinuity topography are given in Dahlen (2005). We can incorporate this information into our tomographic inversion either as explicit constraints in our model parameterization or correct for the effects of variable topography on our GSDF measurements using the exact Fréchet kernels. We are testing both approaches
2. We will increase the upper bound of our inverted frequency range from 50 mHz to 80 mHz. Currently, our synthetics and measurements extend to 80 mHz, but the high-frequency observations are still being evaluated for stability. They have not been included in the models presented here. Once these data have been evaluated (specifically, corrected for the effects of cycle skipping), they will be included in the inversion.

Conclusions

We have developed a comprehensive waveform analysis and inversion scheme to simultaneously estimate 3D variations in shear velocity (β) and shear-wave quality factor Q_μ, and applied this scheme to a large Rayleigh waves dataset sampling eastern Eurasia. The analysis technique characterizes phase and amplitude residuals between recorded and synthetic Rayleigh waves, and inverts them using new three-dimensional sensitivity

(Fréchet) kernels for structural perturbations.   The joint inversion allows us to incorporate the effects of wavefield focusing and scattering on wave amplitudes, improving our ability to resolve variations in attenuation. The analysis spans a frequency band from 0.01-0.05 Hz, with the low frequency estimates providing a stable long-wavelength framework from which we bootstrap to higher frequency. The resulting model provides self-consistent spatial and depth constraints on Q_μ in the crust and upper mantle, with spatial resolution of several hundred kilometers.   Spatial variations of Q_μ observed in the crust generally agree with those observed from higher-frequency crustal phases. Spatial variations in the mantle Q_μ correlate with shear velocity, with high Q_μ lithosphere observed in eastern China, and a low Q_μ region found beneath Tibet. The average attenuation across the region appears to be highly stratified, with a very high Q_μ lithosphere underlain by very low Q_μ in the asthenosphere.

References

Aki, K. & Richards, P. G. (2002). *Quantitative Seismology*, second edition, University Science Books, Sausalito, CA.

Balay S., K. Buschelman, V. Eijkhout, W. D. Gropp, D. Kaushik, M. G. Knepley, L. C. McInnes, B. F. Smith and H. Zhang, 2004. PETSc Users Manual, *ANL-95/11 - Revision 2.1.5, Argonne National Laboratory*. http://www.mcs.anl.gov/petsc

Ben-Menahem, A. and Singh, S. J. (1981). *Seismic Waves and Sources*, Springer-Verlag, New York, NY.

Chen, P (2005). A Unified Methodology for Seismic Waveform Analysis and Inversion. *PhD Dissertation*, University of Southern California.

Chernov, L. A., 1960. *Wave Propagation in a Random Medium*. McGraw-Hill, 168pp.

Constable, S. C., R. L. Parker and C. G. Constable, 1987. Occam's inversion: a practical algorithm for generating smooth models from electromagnetic sounding data. *Geophysics*, **52**, 289-300.

Dahlen, F. A. and Baig, A. M. (2002). Fréchet kernels for body-wave amplitudes, *Geophys. J. Int*. 150: 440-466.

Dahlen, F. A., Hung, S.-H. and Nolet, G. (2000). Fréchet kernels for finite-frequency traveltimes: I. Theory, *Geophys. J. Int*. 141: 157-174.

Dahlen, F. A. (2005). Finite-frequency sensitivity kernels for boundary topography perturbation. *Geophys. J. Int.* 162: 525-540.

Dalton, C.A. and G. Ekstrom (2006). Global models of surface wave attenuation, *J. Geophys. Res.* 111: B05317, doi:10029/2005JB003997.

Dziewonski, A. M. & Anderson, D. L. (1981). Preliminary Reference Earth Model (PREM), *Phys. Earth Planet. Inter.* 25: 297-356.

Gaherty, J.B., T.H. Jordan, and L.S. Gee (1996). Seismic structure of the upper mantle in a central Pacific corridor, *J. Geophys. Res.* 101: 22,291-22,309.

Gee, L. S., and T. H. Jordan (1992). Generalized seismological data functionals, *Geophys. J. Int., 111*, 363-390.

Laske, G., G. Masters, and C. Reif (2001). CRUST 2.0, A New Global Crustal Model at 2x2 Degrees, http://mahi.ucsd.edu/Gabi/rem.html.

Jemborie, A.L. and B.J. Mitchell, (2004). Shear wave *Q* structure and its lateral variation in the crust of China and surrounding regions, *Geophys. J. Int.* 157: 363-380.

Paige, C. C. and M. A. Saunders, 1982. LSQR: sparse linear equations and least squares problems. *ACM Trans. Math. Software,* **8**, 195-209.

Sambridge, M. S., 1990. Non-linear arrival time inversion: constraining velocity anomalies by seeking smooth models in 3-D. *Geophys. J. Int.*, **102**, 653-677.

Snieder R. and A. Lomax., 1996. Wavefield smoothing and the effect of rough velocity perturbations on arrival times and amplitudes. *Geophys J. Int.* **125**, 796-812.

Xie, J. (2006). Pn attenuation beneath Tibetan plateau, *Bull. Seismol. Soc. Am*. submitted.

Xie, J., Z. Wu, R. Liu, D. Schaff, Y. Liu, and J. Liang, 2005. Tomographic regionalization of crustal Lg Q in eastern Eurasia, *Geophys. Res. Lett*., **33**, L03315, doi:10:1029/2005GL024410.

Zhao, L. (2006). Full-wave Fréchet kernels for Q tomography, *in preparation*.

Zhao, L. & T. H. Jordan (2006) Structural sensitivities of finite frequency seismic waves: a full wave approach. *Geophys. J. Int.* 165: 981-990.

Zhao, L., Jordan, T. H. & Chapman, C. H. (2000). Three-dimensional Fréchet differential kernels for seismic delay times, *Geophys. J. Int*. 141: 558-576.

Zhao, L., Jordan, T. H., Olsen, K. B. & Chen, P. (2005). Fréchet kernels for imaging regional Earth structure based on three-dimensional reference models, *Bull. Seismol. Soc. Am*. 95: 2066-2080.

Zhao, L., Chen, P. & Jordan, T. H. (2006). Strain Green's tensor, reciprocity and their applications to seismic source and structure studies. *Bull. Seismol. Soc. Am*. 96: No.5 1753-1763.
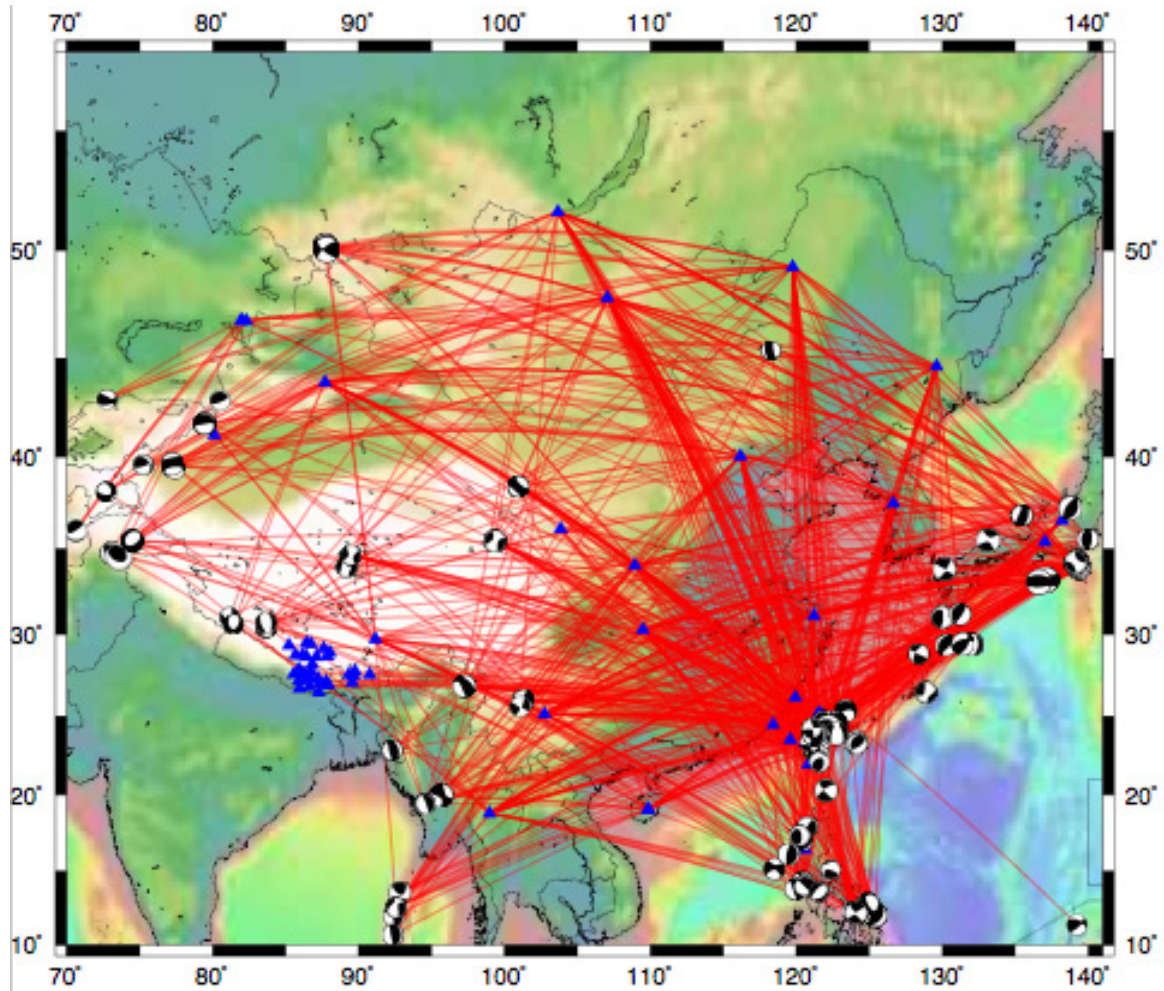
Figure 1. Sour-station path coverage for our current inversion. Harvard CMT solutions are plotted at the epicenters of the earthquakes. Stations are shown as blue triangles. Red lines shows source-station paths used in our inversion.
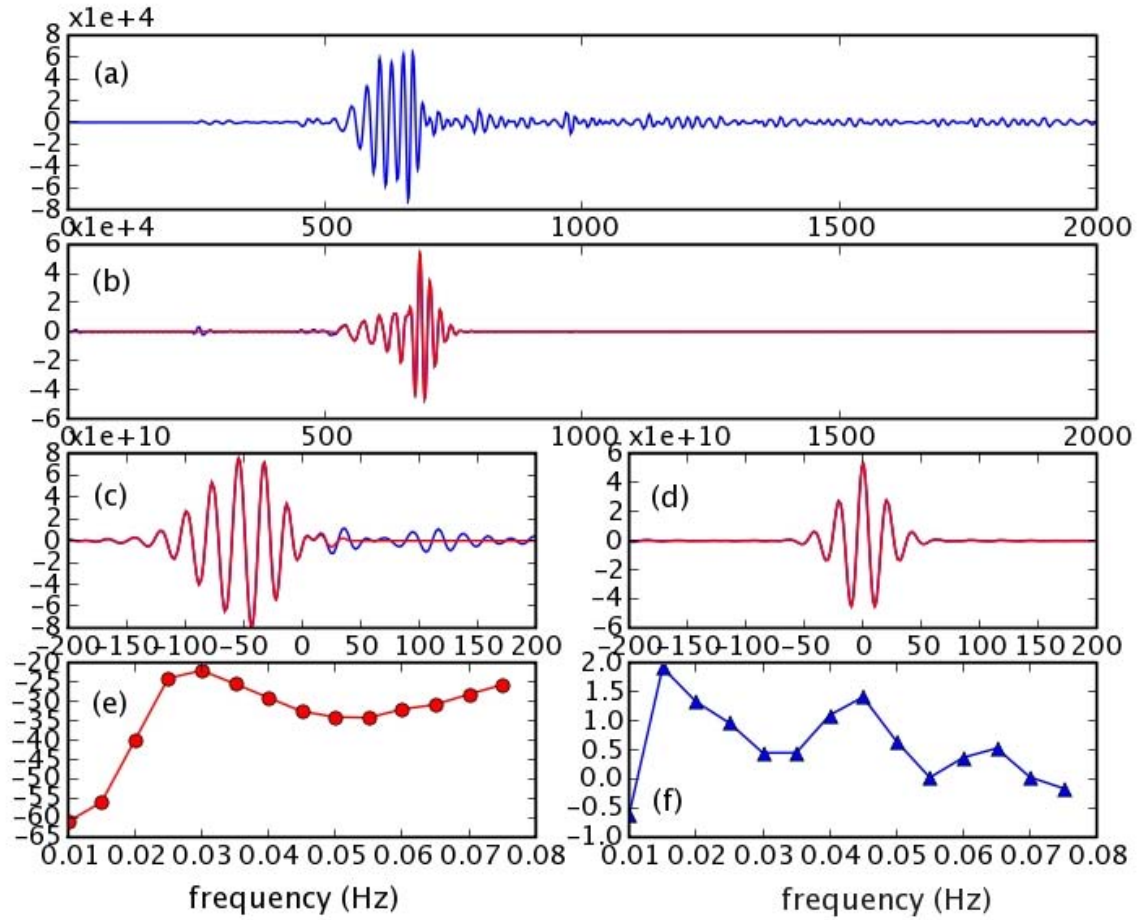
Figure 2. An example of GSDF data processing. (a) observed seismogram; (b) complete synthetic seismogram, the isolation filter is shown in red; (c) cross-correlagram between the isolation filter and the observed seismogram; (d) cross-correlagram between the isolation filter and the complete synthetic seismogram; (e) frequency-dependent phase-delay measurements; (f) frequency-dependent amplitude anomaly measurements.
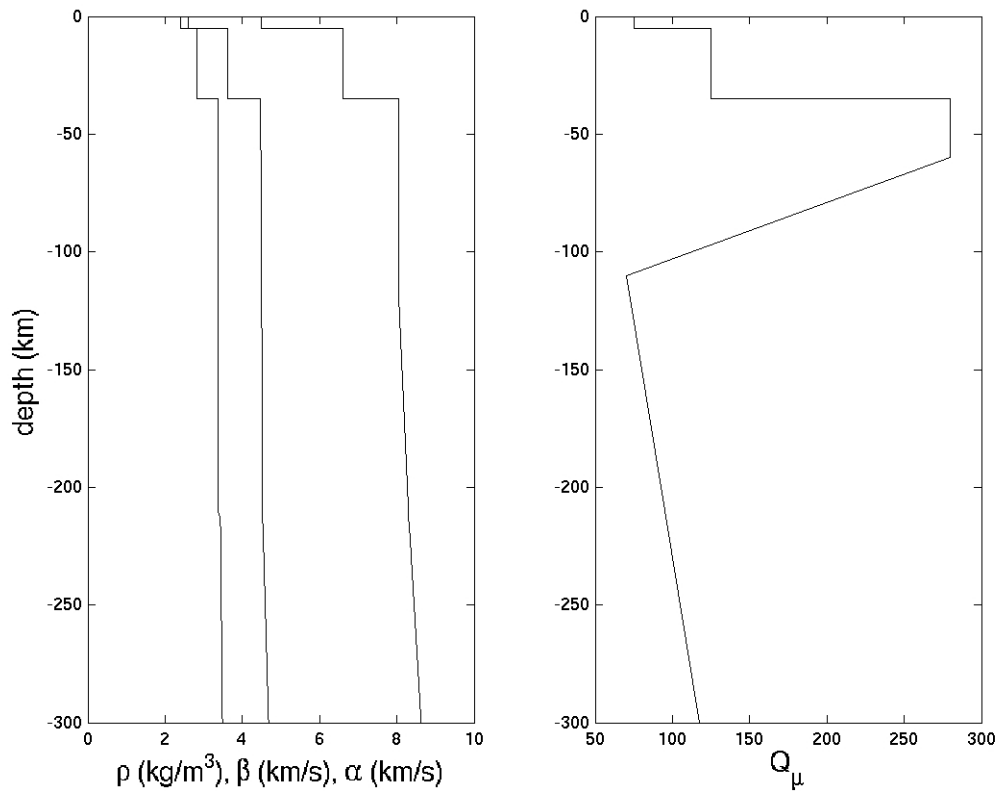
Figure 3. The reference seismic velocity and density models (left) and shear-wave attenuation model (right).
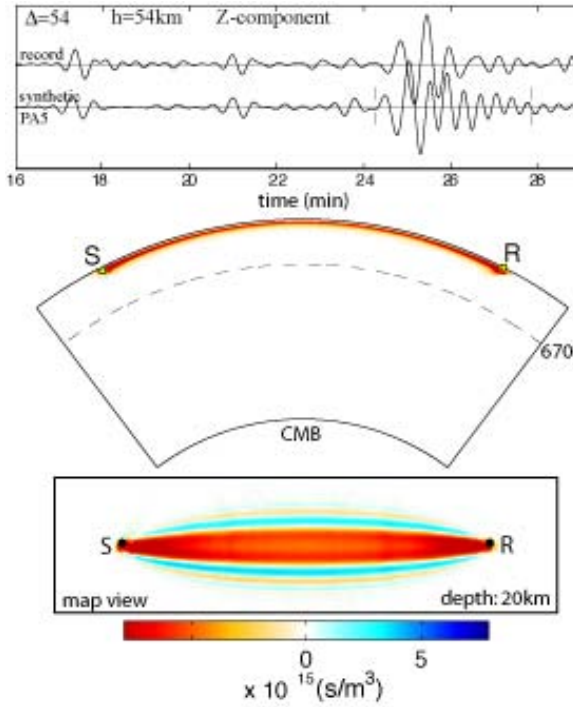
Figure 4(a). Partial derivative kernels for phase-delay with respect to shear velocity, for a typical Rayleigh wave observation. (top panel) Broadband (5-60 mHz) Rayleigh waveform selected for analysis (dashed lines represent window). (middle panel) Cross-section of kernel within the vertical source-receiver plane. (bottom panel) Plan view of kernel at depth 20 km.
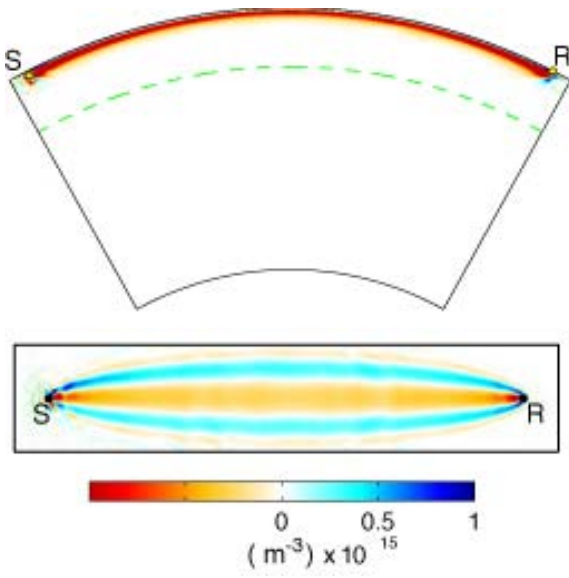
Figure 4(b). Partial derivative kernels for relative amplitude with respect to shear velocity, for the example Rayleigh-wave observation in Figure 1(a). (top panel) Cross-section of kernels within the vertical source-receiver plane. (bottom panel) Plan view of kernel at depth 20 km.
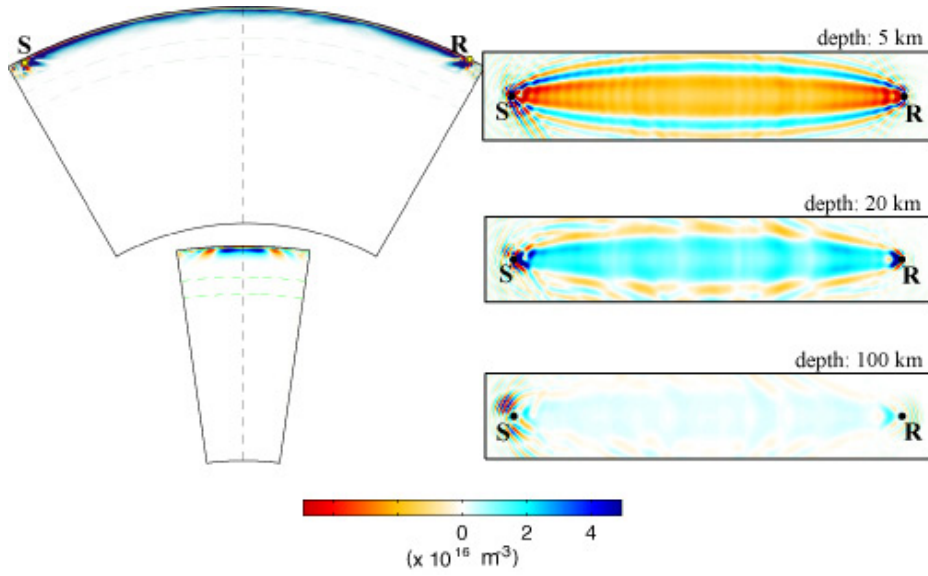
Figure 4(c). Partial derivative kernels for relative amplitude with respect to Q_μ, for the same Rayleigh wave example from Figure 1(a). (left) Cross-sections of kernels within the vertical source-receiver plane, as well as perpendicular to the path, midway between source and receiver. (right) Plan view of kernels at depths of 5, 20, and 100 km. In all kernels, color scale is such that blue indicates regions where an increase in Q_μ will produce an increase in predicted Rayleigh-wave amplitude
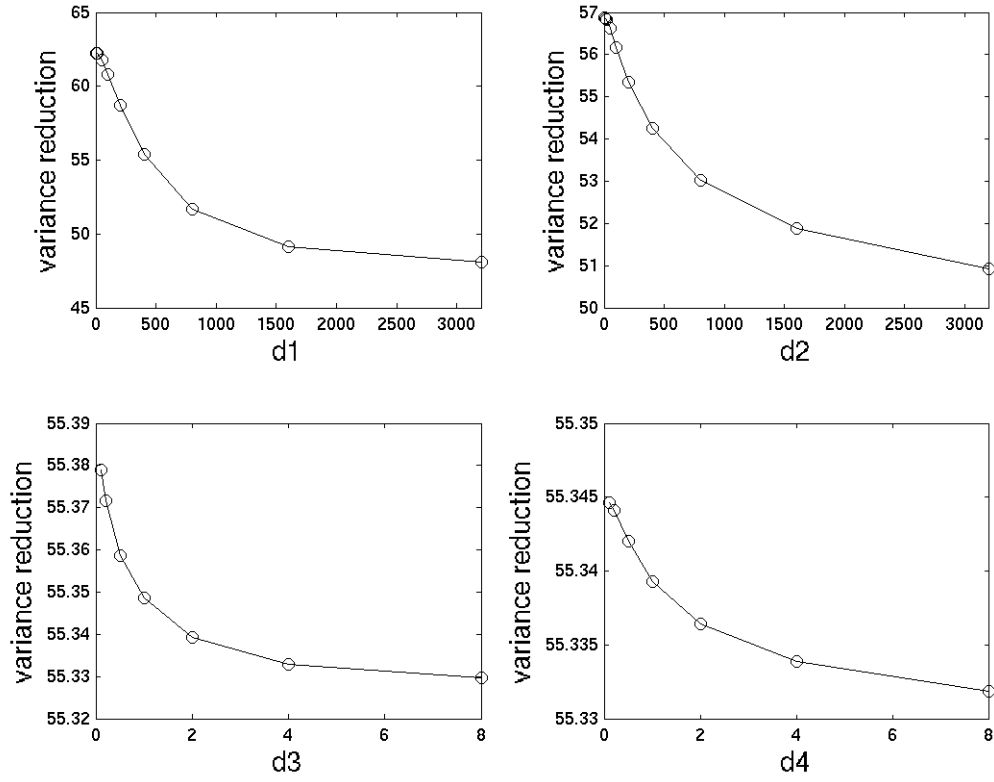
Figure 5. The trade-off relations between model size or smoothness and variance reduction. Variance reduction as a function of the model norm damping parameter θ for shear velocity (a); of the model smoothness damping parameter λ for shear velocity (b); of the model norm damping parameter θ for Q_μ (c); of the model smoothness damping parameter λ for Q_μ.
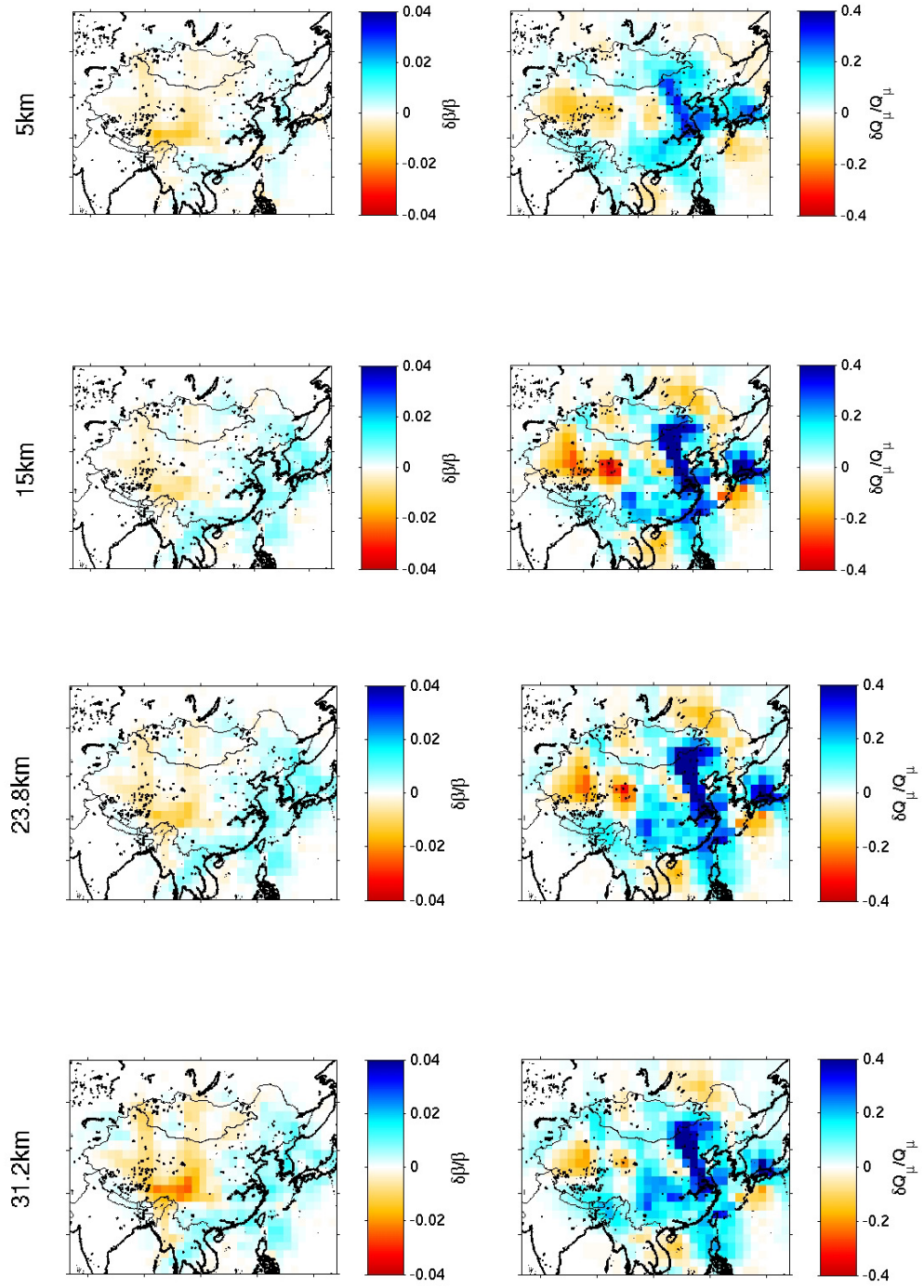
Figure 6(a) Shear-velocity perturbation (left) and attenuation perturbation (right) at 5 km to 31 km depths.
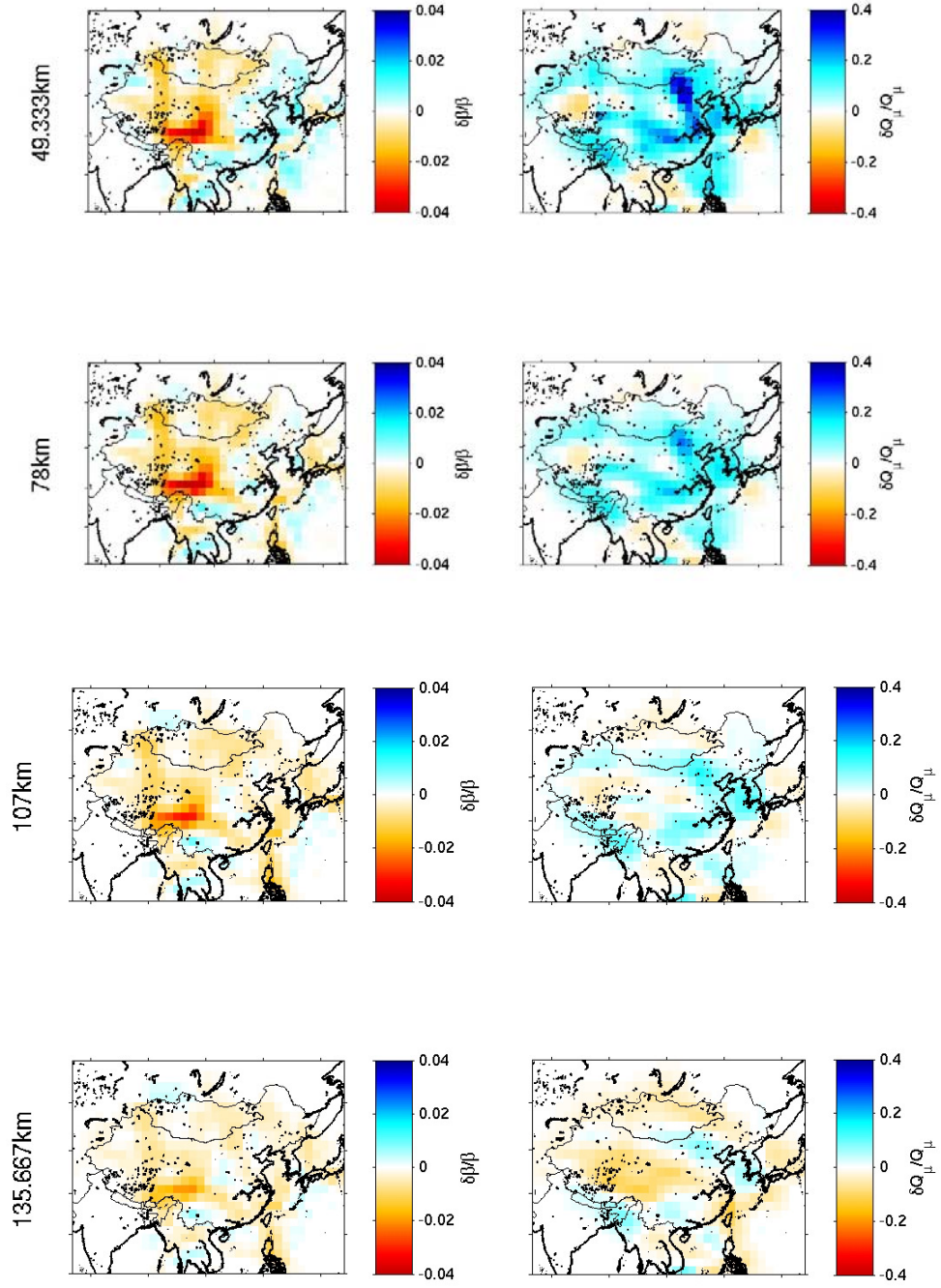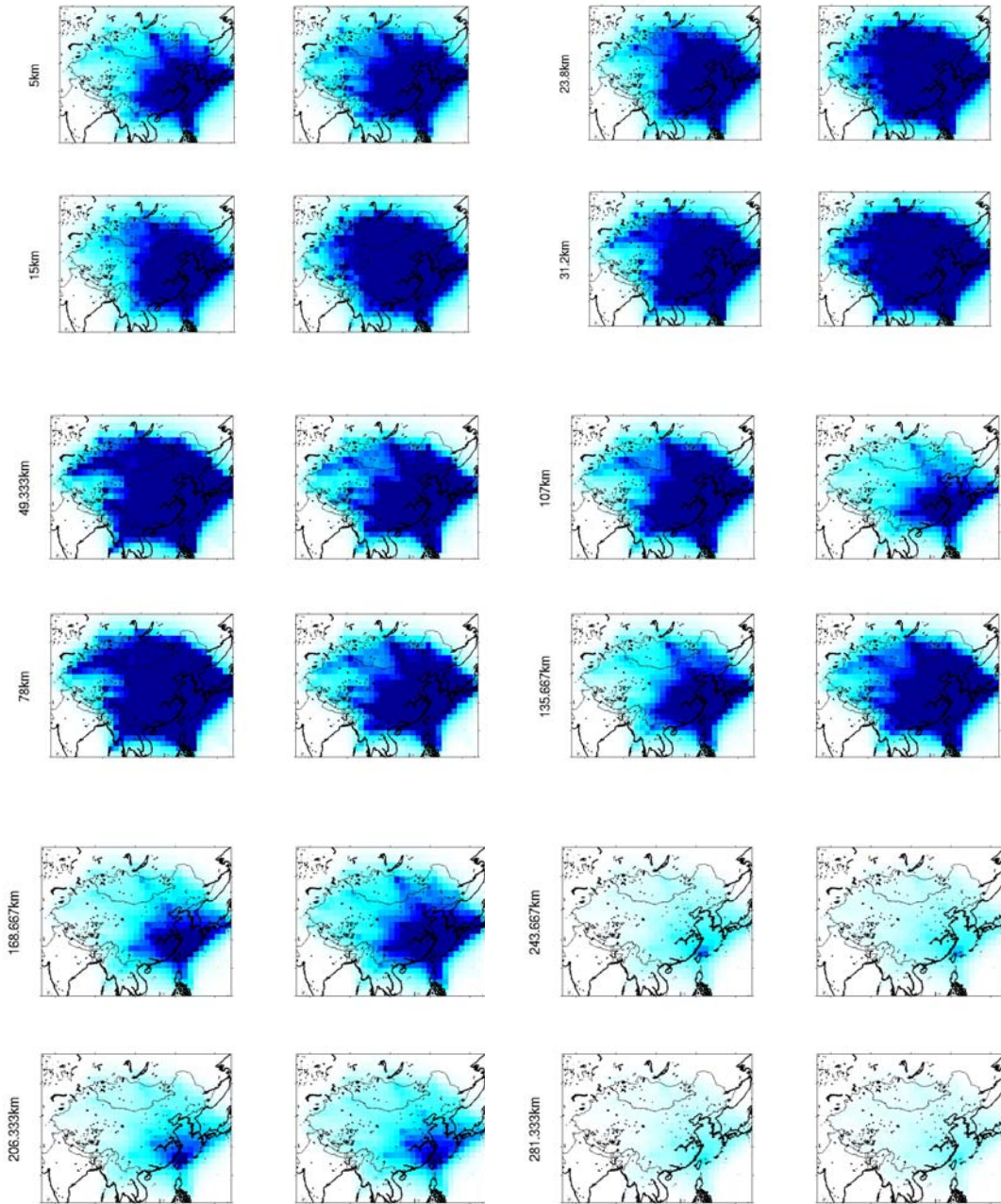
Figure 6(b) Shear-velocity perturbation (left) and attenuation perturbation (right) at 49 km to 136 km depths.
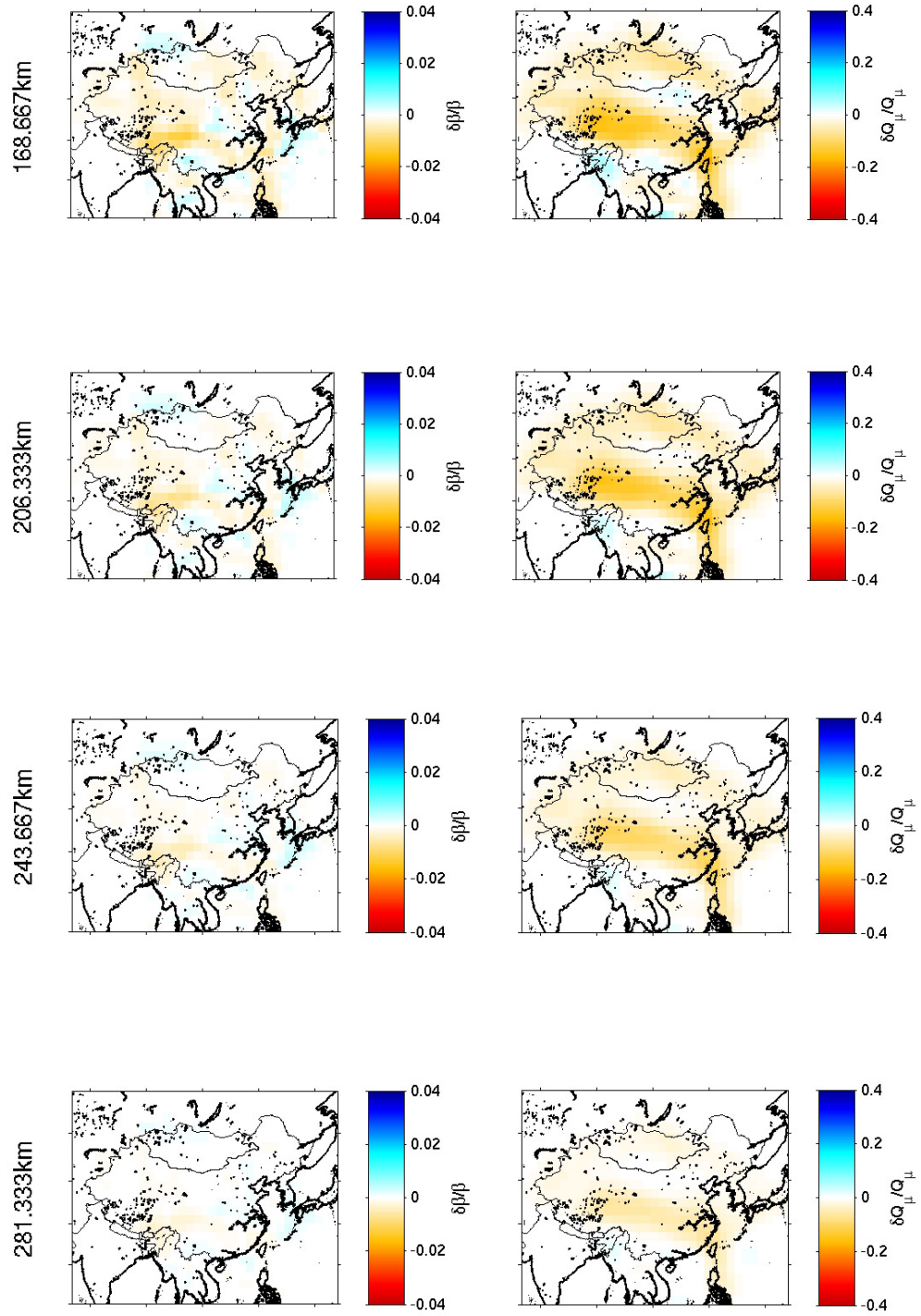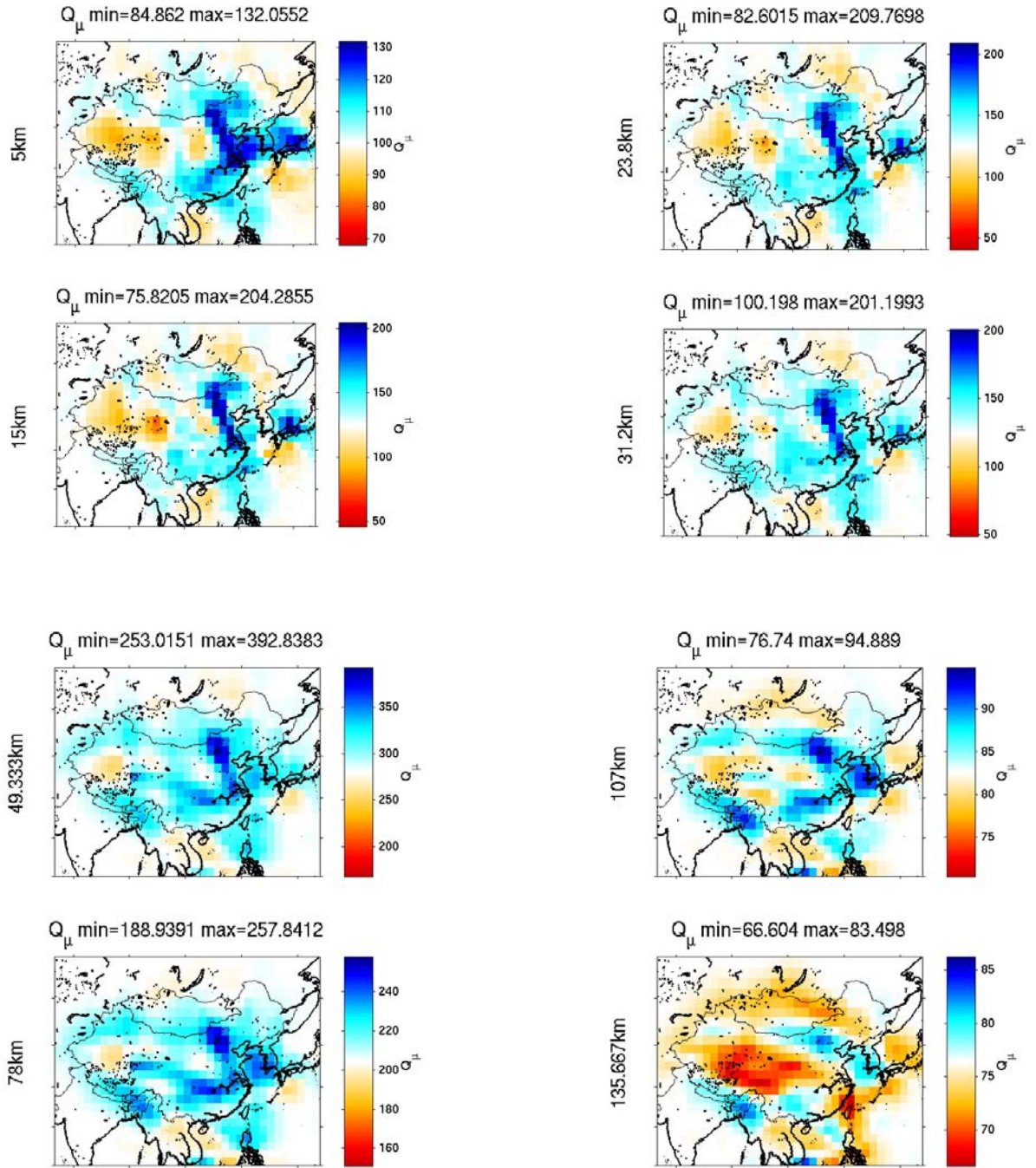
Figure 6(c) Shear-velocity perturbation (left) and attenuation perturbation (right) at 206 km to 281 km depths.
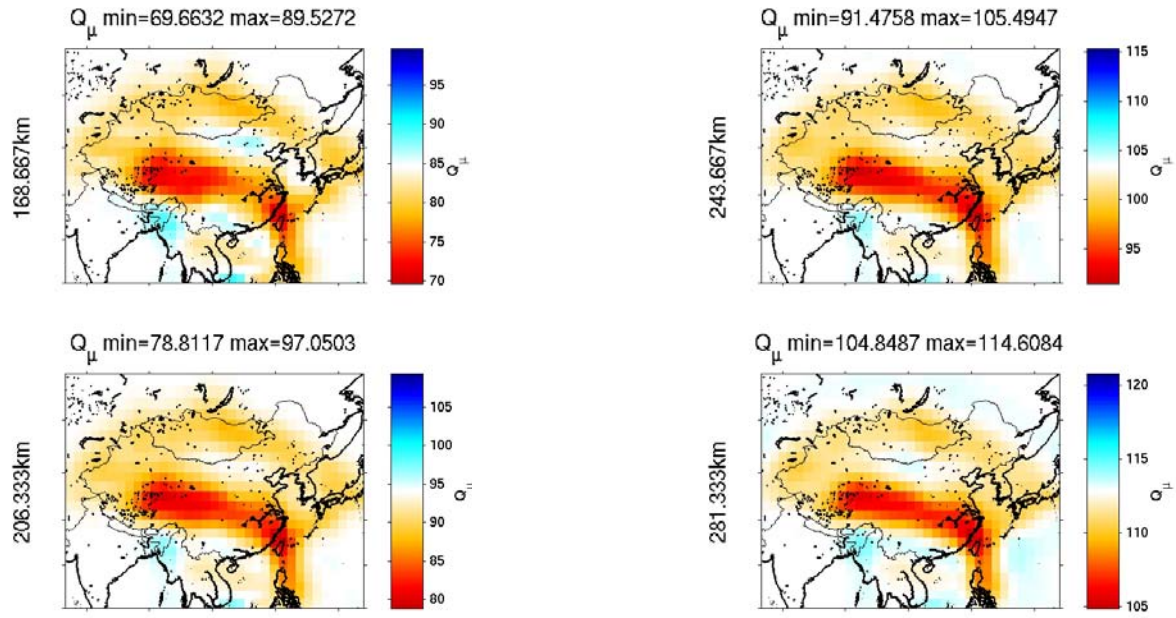
Figure 7 Kernel coverage at 12 different depths. First and third columns: coverage of shear-velocity kernels; second and fourth columns: coverage of attenuation kernels.

Figure 8(a) The updated 3D shear-wave attenuation model for eastern Eurasia obtained by applying the 3D perturbation (Figure 6) to the 1D reference model, for depths of 5-135 km.

Figure 8(b) The updated 3D shear-wave attenuation model for eastern Eurasia obtained by applying the 3D perturbation (Figure 6) to the 1D reference model, for depths of 169-281 km.